Title: *Seasonality in aerodynamic resistance across a range of North American ecosystems*

Authors:

Adam M. Young[1,2,*], Mark A. Friedl[3], Bijan Seyednasrollah[1,2], Eric Beamesderfer[1,2], Carlos M. Carrillo[4], Xiaolu Li[4], Minkyu Moon[3], M. Altaf Arain[5], Dennis D. Baldocchi[6], Peter D. Blanken[7], Gil Bohrer[8], Sean P. Burns[7,9], Housen Chu[10], Ankur R. Desai[11], Timothy J. Griffis[12], David Y. Hollinger[13], Marcy E. Litvak[14], Kim Novick[15], Russell L. Scott[16], Andrew E. Suyker[17], Joseph Verfaillie[6], Jeffrey D. Wood[18], and Andrew D. Richardson[1,2]

Affiliations:

[1]School of Informatics, Computing, and Cyber Systems, Northern Arizona University, Flagstaff, AZ 86011

[2]Center for Ecosystem Science and Society, Northern Arizona University, Flagstaff, AZ 86011

[3]Dept. Earth and Environment, Boston University, Boston, MA 02215

[4]Dept. Earth and Atmospheric Sciences, Cornell University, Ithaca, NY 14853

[5]School of Earth, Environment & Society and McMaster Centre for Climate Change, McMaster University, Hamilton, ON, Canada

[6]Department of Environmental Science, Policy and Management, University of California, Berkeley, CA 94720

[7]Department of Geography, University of Colorado, Boulder, CO 80309

[8]Department of Civil, Environmental and Geodetic Engineering, The Ohio State University, Columbus, OH 43210

[9]National Center for Atmospheric Research, Boulder, Colorado, 80301

[10]Lawrence Berkeley National Laboratory, Berkeley, CA 94702

[11]Dept of Atmospheric and Oceanic Sciences, University of Wisconsin-Madison, Madison, WI 53706

[12]Department of Soil, Water, and Climate, University of Minnesota, Saint Paul, MN, 55108

[13]Northern Research Station, USDA Forest Service, Durham, NH 03824

[14]Biology Department, University of New Mexico, Albuquerque, NM 87107

[15]O'Neill School of Public and Environmental Affairs, Indiana University - Bloomington. Bloomington, IN, 47408

[16]Southwest Watershed Research Center, USDA-Agricultural Research Service, Tucson, AZ, USA

[17]School of Natural Resources, University of Nebraska, Lincoln, NE 68583

[18]School of Natural Resources, University of Missouri, Columbia, MO 65211

*Corresponding author: adam.young@nau.edu

Keywords: phenology, AmeriFlux, PhenoCam, aerodynamic resistance, land-atmosphere interactions, sensible heat flux

Abstract

Surface roughness – a key control on aerodynamic resistance and thereby land-atmosphere exchanges of heat and momentum – differs between dormant and growing seasons and accompanies changes in canopy greenness and leaf area. However, how surface roughness shifts seasonally at fine time scales (e.g., days) in response to seasonality in canopy conditions is not well understood. This study: (1) explores how and where aerodynamic resistance changes seasonally; (2) what drives these seasonal shifts in aerodynamic resistance, including the role of vegetation phenology; and (3) quantifies the importance of including seasonal changes of aerodynamic resistance in "big leaf" models of sensible heat flux (H). We evaluated aerodynamic resistance and surface roughness lengths for momentum (z_{0m}) and heat (z_{0h}) using the kB^{-1} parameter ($\ln(z_{0m}/z_{0h})$), derived from Monin-Obukhov Similarity Theory. We used AmeriFlux data to obtain surface-roughness estimates, and PhenoCam greenness data for phenology. This analysis spanned a continental-scale precipitation and temperature gradient, including 23 sites and ~190 site years from deciduous broadleaf, evergreen needleleaf, woody savanna, cropland, grassland, and shrubland plant-functional types (PFT). Results indicated clear seasonal patterns in aerodynamic resistance to sensible heat transfer (R_{ah}). This seasonality tracked PhenoCam-derived start-of-season green-up transitions in PFTs displaying the most significant seasonal changes in canopy leaf area, with R_{ah} decreasing near the green-up transition. Conversely, in woody savanna sites and evergreen needleleaf forests, there were strong seasonal patterns in R_{ah} at some sites, but these patterns were not linked to vegetation green-up. Our findings highlight that decreases in kB^{-1} are an important control over R_{ah}, explaining > 50% of seasonal variation in R_{ah} across most sites. Decreases in kB^{-1} during green-up are likely caused by increasing z_{0h} in response to higher leaf area index and not to seasonal changes in z_{0m}.

Accounting for seasonal variation in kB^{-1} is also key for predicting H as well; assuming kB^{-1} to be constant at each site resulted in significant biases that also exhibited strong seasonal patterns between estimated and measured H (i.e., $\hat{H}/H$). Overall, we found that in ecosystems with strong seasonality in leaf area, surface roughness can be sensitive to phenology, and this linkage is therefore critical for understanding land-atmosphere interactions at seasonal time scales.

1. Introduction

The horizontal and vertical structure of vegetation creates an aerodynamically rough surface, generating mechanical turbulence that exerts significant control over aerodynamic resistance to heat transfer from the surface to the atmosphere (Brutsaert, 1982; Garratt and Hicks, 1973; Pitman, 2003; Verma, 1989). Surface roughness varies with wind speed (Thom 1972), land cover type (Lee et al., 2011), leaf area (Dolman, 1986; Raupach, 1994; Shaw and Pereira, 1982), and canopy height (Chu et al., 2018; Sonnentag et al., 2011), such that changes in vegetation structure lead to significant changes in aerodynamic resistance. Vegetation phenology triggers significant and rapid changes in the structure of the canopy (Richardson et al., 2013), altering surface roughness during green-up and senescence. Such phenology-driven impacts can influence the land-surface energy balance by changing aerodynamic resistance and hence sensible heat flux (H), in addition to other key biophysical processes such as evapotranspiration (Fitzjarrald et al., 2001; Moon et al., 2020; Schwartz, 1992). Capturing dynamics between phenology and aerodynamic resistance is therefore critical for accurately parameterizing the role of phenology in land-surface models (e.g., Richardson et al., 2012). More broadly, phenology driven changes in aerodynamic resistance can impact on the atmospheric boundary-layer, including temperature profile development, boundary-layer height and cloud formation, and near-surface micro-climate (Baldocchi and Ma, 2013; Betts, 2004; Novick and Katul, 2020).

The magnitude of H is controlled by the difference between surface and air temperatures and the aerodynamic resistance to sensible heat transfer. Modeling and predicting aerodynamic resistance requires information on two key surface-roughness parameters: roughness lengths for momentum and heat (Verhoef et al., 1997). The roughness length for momentum (z_{0m}) defines the height above the surface that wind speed extrapolates to zero, and the roughness length for

89 heat (z_{0h}) is the effective source height in the vertical temperature profile for sensible heat. In
90 ecosystems with taller roughness obstacles (e.g., forests), an additional parameter is commonly
91 needed: the zero-plane displacement height (d). Under such conditions, wind speed extrapolates
92 to zero at height $d + z_{0m}$. Differences between z_{0m} and z_{0h} result in an "excess resistance" to heat
93 transfer relative to momentum transfer. Specifically, heat transfer from $z_{0h} \rightarrow z_{0m}$ is dominated
94 by molecular diffusion, while heat transfer above z_{0m} is controlled by more efficient processes
95 associated with eddy diffusion (Bonan, 2016; Thom, 1972). In land-surface modeling, the
96 parameter kB^{-1} ($\ln(z_{0m}/z_{0h})$) is used to quantify this excess resistance between z_{0m} and z_{0h}
97 (Brutsaert, 1982; Owen and Thomson, 1963; Thom, 1972). Further details on the derivation of
98 excess resistance and kB^{-1} are found in Section 2.1.

99 The kB^{-1} parameter varies significantly with land-cover type, leaf area, and other
100 environmental variables (Brutsaert, 1982; Rigden et al., 2018). For example, a deciduous
101 broadleaf forest acts as a permeable-rough surface, defined as having densely packed, porous
102 elements and exhibiting relatively low kB^{-1} values (kB^{-1} generally ranges from 0-4). Conversely,
103 in arid ecosystems, the canopy is characterized by uneven and sparse roughness elements (i.e., a
104 bluff-rough surface), and kB^{-1} generally exhibits higher values (kB^{-1} ranges from 2-10) (Rigden et
105 al., 2018). For bare soil, kB^{-1} has low values (ranging from 0-1), and negative kB^{-1} values have
106 also been estimated (Yang et al., 2008). This variability in kB^{-1} among differing land cover is
107 also clearly illustrated by the bifurcation of kB^{-1} among land-cover types, with higher values
108 occurring in bluff-rough surfaces compared to permeable-rough surfaces (Garratt and Hicks,
109 1973; Rigden et al., 2018), implying differences in the physical arrangement and structure of
110 surface-roughness elements strongly governs behavior of kB^{-1}. While this bifurcation is well
111 documented among varying land-cover, little work exists exploring seasonal changes in kB^{-1},

which may in part be driven by changes in canopy structure, including the amount and distribution of leaf area.

kB^{-1} displays strong temporal variability in response to multiple different environmental factors. At a diurnal scale for sparse canopies, solar radiation penetrates below the canopy, warming the soil, and causing z_{0h} to be effectively the height of the soil surface, thereby increasing kB^{-1}. Meanwhile, z_{0m} is constant at daily time scales (Brutsaert and Sugita, 1996; Kustas et al., 1989; Verhoef et al., 1997). At a seasonal time scale, some evidence suggests that changing leaf area over time causes a distinct negative relationship between leaf area index and kB^{-1} (Qualls and Brutsaert, 1996). These patterns can also be generalized at different time scales. Conceptually (Fig. 1), daily kB^{-1} peaks at midday as the diurnal cycle in solar radiation causes the magnitude of the temperature gradient at the top of the canopy to increase, ultimately altering z_{0h}. Similarly, the impact of vegetation green-up can also cause kB^{-1} to vary at seasonal time scales. For example, changes in z_{0h} may effectively track changes in z_{0m}, leading to a constant kB^{-1} for the entire season. Conversely, z_{0h} may increase faster relative to z_{0m}, leading to decreases in kB^{-1} during green-up transitions (Fig. 1).

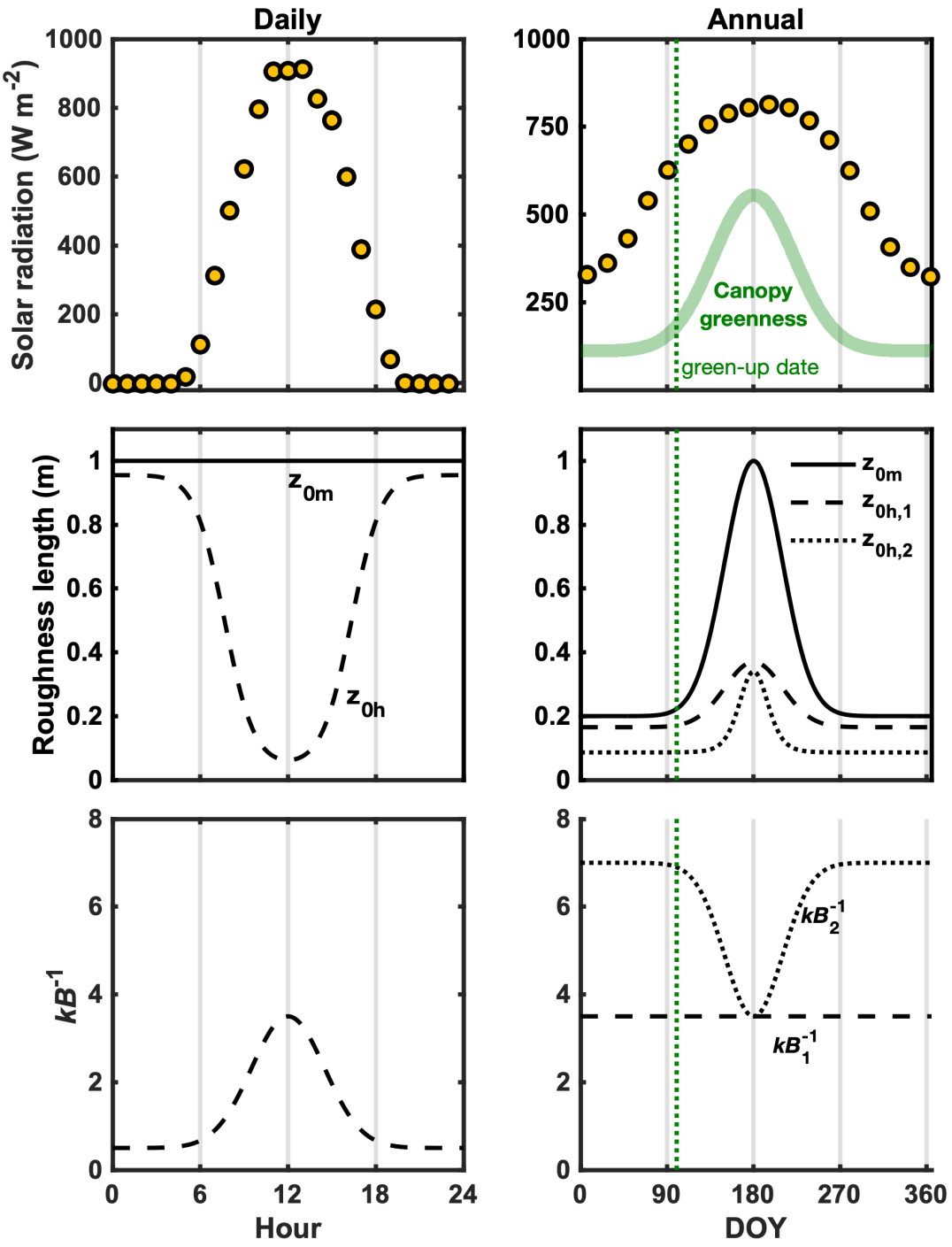

Figure 1. Hypothesized behavior of kB^{-1} at multiple time scales. The left column of panels displays idealized diurnal behavior for short-statured vegetation at DOY 180 and how solar radiation may cause shifts in z_{0h} and kB^{-1}. Panels on the right-hand side depict behavior of kB^{-1} at a seasonal time scale. At seasonal time scales, the behavior of z_{0m} and z_{0h} relative to each other will determine kB^{-1}. Two different potential behaviors are depicted above. The dashed curve ($z_{0h,1}$) represents a potential scenario where z_{0h} proportionally tracks z_{0m} resulting in a constant kB^{-1} for the entire year. Alternatively, the dotted curve ($z_{0h,2}$) represents a scenario where z_{0h} increases faster relative to z_{0m} in response to green-up, resulting in a decrease in kB^{-1}. The faded green line represents canopy greenness while the vertical line indicates a theoretical green-up date.

Determining whether changes in z_{0m} or z_{0h} are the primary driver of seasonal variation in kB^{-1} is critical for identifying the biophysical drivers of aerodynamic resistance. A simple – and common – approach is to equate z_{0m} as a fraction of mean canopy height (h_c) (e.g., $z_{0m} = 0.1h$; Bonan, 2016). d is similarly estimated as $d = 0.7h_c$. However, while this is a common method for estimating these roughness parameters, this approach has several important limitations. First, this approach cannot produce time series of changes in z_{0m} unless continuous measurements of h_c are recorded. Second, seasonal signals in z_{0m} are complex and may not effectively track canopy height. For example, as the canopy fills in after leaf emergence, z_{0m} may display non-monotonic variation with leaf area, increasing in length before decreasing (Shaw and Pereira, 1982). Additionally, as leaf area increases, the coefficients mapping h_c to z_{0m} and d (e.g., $z_{0m}/h_c = 0.1$ and $d/h_c = 0.7$) are not constant and can decrease and increase, respectively (Sakai, 2000). Measurements of wind speed and turbulence from flux towers offer an alternative method for estimating z_{0m}. For example, if wind speed is available at multiple heights above the canopy, a vertical wind-speed profile can result, allowing for extrapolation of d and z_{0m} (Monteith and Unsworth, 2008), and a similar approach may be used for z_{0h} using air temperature profiles. At towers where measurements are available at only one height, an effective or "aerodynamic" canopy height can be estimated using Monin-Obukhov similarity theory, and thereby allow for inference into changes in of d and z_{0m} (Chu et al., 2018; Pennypacker and Baldocchi, 2016). However, this approach requires explicit assumptions regarding d/h_c and z_{0m}/h_c. More details regarding Monin-Obukhov similarity theory and estimating z_{0m} and d can be found in sections 2.1 and 2.6.

Common approaches to parameterizing kB^{-1} in predictions of H include simple assumptions. One such assumption is $z_{0m} = z_{0h}$ (i.e., $kB^{-1} = 0$) (Campbell and Norman, 1998). While assuming

159 $kB^{-1} = 0$ simplifies calculations of H, it can cause significant bias (Yang et al., 2008), and is
160 therefore not commonly used. Another approach is to assume kB^{-1} is a non-zero constant. For
161 example, $kB^{-1} \approx 2$ is a common assumption, and shows good performance during the growing
162 season for agricultural and forested land-cover types (Garratt and Francey, 1978; Zhao et al.,
163 2016).

164 Despite extensive literature focused on kB^{-1}, few studies have explored how aerodynamic
165 resistance changes seasonally, what drives these changes, and what the consequences are of such
166 variation in aerodynamic resistance for predicting seasonal patterns in H (e.g., Moon et al., 2020;
167 Sugita and Kubota, 1994). Furthermore, estimates of H from vegetated surfaces in land-surface
168 models directly rely on model assumptions linking surface roughness to changes in leaf area and
169 canopy height, further motivating the need for clearer understanding of how phenology may
170 influence surface roughness (Lawrence et al., 2018; Zeng and Wang, 2007). Here, we address the
171 following questions: (1) how does aerodynamic resistance change at seasonal time scales across
172 a range of plant functional types and climate regimes, (2) what are the mechanisms that lead to
173 changes in aerodynamic resistance, including the role of plant phenology, and (3) how does
174 assuming kB^{-1} to be constant influence estimates of H at seasonal time scales? To address these
175 questions, we analyzed data from 23 sites that are part of both the AmeriFlux and PhenoCam
176 networks, covering deciduous broadleaf, evergreen needleleaf, cropland, grassland, woody
177 savanna, and shrubland land-cover types, and spanning a broad climatological gradient across
178 North America.

2. Materials and methods

2.1 Basic theory

Whole ecosystem H is commonly modeled using a "big leaf" approach, which considers that ecosystems behave as a single layer, and therefore does not account for vertical differences from the soil through the canopy (Knauer et al., 2018; Raupach and Finnigan, 1988). Under this "big leaf" approach, H is a function of the difference between the aerodynamic surface temperature (T_{aero}) and air temperature at tower height (T_a), as well as aerodynamic resistance to heat transfer (R_{ah}):

$$H = \frac{\rho c_p (T_{aero} - T_a)}{R_{\mathrm{ah}}} \quad (1)$$

where ρ is air density (kg m^{-3}) and c_p is a constant for the specific heat of dry air (1004.834 J K^{-1} kg^{-1}). The total aerodynamic resistance to heat transfer (R_{ah}; s m^{-1}) is the sum of the resistance to momentum transfer (R_{am}) and an excess resistance term (R_{bh}) representing differences between roughness lengths for momentum (z_{0m}) and heat (z_{0h}),

$$R_{\mathrm{ah}} = R_{\mathrm{am}} + R_{\mathrm{bh}} \quad (2)$$

To calculate R_{ah}, R_{am}, and R_{bh}, we used the methods described by Verma (1989) and published in the *'bigleaf'* R package (Knauer et al., 2018). Specifically, we estimated R_{am} using the definition:

$$R_{\mathrm{am}} = u/u_*^2 \quad (3)$$

where u and u_* are tower-measured horizontal wind speed (m s^{-1}) and friction velocity (m s^{-1}), respectively. The excess resistance, R_{bh}, is defined as:

$$R_{\mathrm{bh}} = \frac{1}{k u_*}\left[\ln\left(\frac{z_{0m}}{z_{0h}}\right) - \psi_h + \psi_m\right] \quad (4)$$

Here, k is the unitless von Kármán constant (0.41), and ψ_m and ψ_h are stability functions for momentum and heat exchange using formulations from Dyer (1970) and Businger et al. (1971).

Following Rigden et al. (2018) and Verma (1989), we used the common, simplified definition of R_{bh} ignoring stability effects over the short distance $z_{0m} \rightarrow z_{0h}$:

$$R_{bh} = \frac{1}{ku_*} \ln\left(\frac{z_{0m}}{z_{0h}}\right) \quad (5)$$

We tested the impact of not including stability effects when estimating R_{bh} using Eqn. 5 and found that this only had minor impacts on our results (Fig. S1). The kB^{-1} parameter characterizes differences between z_{0m} and z_{0h}, and is defined as:

$$kB^{-1} = \ln\left(\frac{z_{0m}}{z_{0h}}\right) \quad (6)$$

Substituting Eqns. 5 and 6 yields:

$$R_{bh} = \frac{1}{ku_*} kB^{-1} \quad (7)$$

kB^{-1} has been well studied across a broad range of ecosystems but cannot be measured directly. Multiple methods have been proposed to model and estimate kB^{-1}. These methods range from simple functions of u_* or the roughness Reynolds number (Re_*) (Brutsaert, 1982; Rigden et al., 2018; Thom, 1972; Verhoef et al., 1997), to more complex models that account for variation in the vertical and horizontal distribution of vegetation (Massman, 1999; Yang and Friedl, 2003). Here, our goal was to better understand the seasonality of kB^{-1}, and therefore we did not develop new prognostic models for kB^{-1}. Instead, we focused on estimating kB^{-1} by optimizing the value that best predicted tower-measured H at relatively fine time scales (i.e., 3-days). Further details can be found in Section 2.4.

2.2 Tower data

We used eddy covariance measurements from 23 AmeriFlux sites that also had PhenoCams. These sites were selected because they spanned a broad gradient in climate and vegetation structure across North America, while also having a minimum of two years of overlap between

AmeriFlux and PhenoCam data records. Mean annual temperatures ranged from 1.5 to 17.6 °C and mean annual precipitation ranged from 275 to 2452 mm. Growing season canopy heights ranged from 0.3 m in the US southwest to 60 m in the US northwest and leaf area index (LAI, m^2 m^{-2}) ranged from 0.3 to 8.7 (Table 1). While we required a two-year minimum overlap between AmeriFlux and PhenoCam, we used a longer time series of tower measurements based on data availability and continuity. For each site, we used measurements of precipitation, net radiation (R_n), T_a, H, and u_*. We used radiometric surface temperature (T_s) as a proxy for T_{aero} (Eqn. 1). T_s was computed using separate measurements of upwelling (R_{lu}) and downwelling (R_{ld}) longwave radiation,

$$T_s = \sqrt[4]{\frac{R_{lu} - (1-\varepsilon)R_{ld}}{\varepsilon\sigma}} \quad (8)$$

Here, ε is emissivity and σ is the Stefan-Boltzmann constant (5.67×10^{-8} W m^{-2} K^{-4}). Emissivity values for each vegetation type were obtained from Tao et al. (2013). Hour or half-hour tower data were filtered for mid-day only (10:00-14:00 local time) with $R_n > 50$ W m^{-2}, $H > 50$ W m^{-2}, and $u_* > 0.2$ m s^{-1}. Days with lower R_n were excluded to remove measurements with proportionally higher uncertainty (i.e., $R_n < 50$ W m^{-2}) (Hollinger and Richardson, 2005). We included a filter for H (i.e., $H < 50$ W m^{-2}) to remove anomalously high values of kB^{-1} obtained through our optimization approach when H is near zero. We excluded low u_* values to remove observations having insufficient turbulence (Papale et al., 2006). Finally, we excluded days where any precipitation was recorded between 20:00 hr the previous day to 14:00 hr of the current day. All tower data were downloaded from the AmeriFlux server (https://ameriflux.lbl.gov), and dataset version numbers and download dates are provided in Table S1.

Table 1. AmeriFlux and PhenoCam sites used in this study, including primary plant functional type (PFT), geographic coordinates, elevation, mean annual temperature (MAT) and precipitation (MAP), and mean growing season leaf area index (LAI), mean canopy height (h_c), and whether the site provides profile data for wind speed (u) or air temperature (T_a). (PFT codes: DBF = deciduous broadleaf forest, ENF = evergreen needleleaf forest, GRA = grassland, OSH = open shrublands, WSA = woody savanna, and CRO = croplands or agricultural sites)

Site	PhenoCam	PFT	Lon.	Lat.	MAT (°C)	MAP (mm)	LAI (m^2 m^{-2})	h_c (m)	Profile data? (u/T_a)	Reference	Dataset DOI
CA-TP4	turkeypointenf39	ENF	-80.35	42.71	8.0	1036	8.0	22.0	No/Yes	Peichl et al., 2010	10.17190/AMF/1246012
US-Bi1	bouldinalfalfa	CRO	-121.50	38.10	16.0	338	3.0	0.8	No/No	Hemes et al., 2019	10.17190/AMF/1480317
US-Ho1	howland1	ENF	-68.74	45.20	5.3	1070	5.7	20.0	No/No	Richardson and Hollinger, 2005	10.17190/AMF/1246061
US-Me2	oregonMP	ENF	-121.56	44.45	6.0	523	3.0	16.5	No/Yes	Thomas et al., 2009	10.17190/AMF/1246076
US-Me6	oregonYP	ENF	-121.61	44.32	7.6	494	1.3	6.5	No/Yes	Ruehr et al., 2014	10.17190/AMF/1246128
US-MMS	morganmonroe	DBF	-86.41	39.32	10.9	1032	4.6	27.0	Yes/Yes	Roman et al., 2015	10.17190/AMF/1246080
US-MOz	missouriozarks	DBF	-92.20	38.74	12.1	986	3.9	24.2	No/No	Gu et al., 2016	10.17190/AMF/1246081
US-Mpj	usmpj	WSA	-106.24	34.44	10.5	385	1.1	2.7	No/No	Anderson-Teixeira et al., 2011	10.17190/AMF/1246123
US-Ne1	mead1	CRO	-96.48	41.17	10.1	790	5.5 (c)	3.0	Yes/Yes	Suyker and Verma, 2010	10.17190/AMF/1246084
US-Ne2	mead2	CRO	-96.47	41.16	10.1	789	5.3 (c) 5.0 (s)	3.0 1.0	Yes/Yes	Suyker and Verma, 2012	10.17190/AMF/1246085
US-Ne3	mead3	CRO	-96.44	41.18	10.1	784	4.2 (c) 4.0 (s)	2.7 0.9	Yes/Yes	Suyker and Verma, 2012	10.17190/AMF/1246086
US-NR1	niwot3	ENF	-105.55	40.03	1.5	800	3.7	11.4	No/Yes	Burns et al., 2015	10.17190/AMF/1246088
US-Ro4	rosemountnprs	GRA	-93.07	44.68	6.4	879	3.0	1.5	No/No	Markland, 2019	10.17190/AMF/1419507
US-Ses	sevilletashrub	OSH	-106.75	34.34	13.7	275	0.3	0.6	No/No	Petrie et al., 2015	10.17190/AMF/1246125
US-Syv	sylvania	DBF	-89.38	46.24	3.8	826	4.0	24.8	Yes/Yes	Desai et al., 2005	10.17190/AMF/1246106
US-Ton	tonzi	WSA	-120.97	38.43	15.8	559	0.7	10.0	Yes/Yes	Ma et al., 2016	10.17190/AMF/1245971
US-Tw3	twitchellalfalfa	CRO	-121.65	38.12	15.6	421	3.0	0.8	No/No	Oikawa et al., 2017	10.17190/AMF/1246149
US-UMB	umichbiological	DBF	-84.71	45.56	5.8	803	5.8	23.0	No/No	Gough et al., 2013	10.17190/AMF/1246107
US-Var	vaira	GRA	-120.95	38.41	15.8	559	3.5	0.3	No/No	Ma et al., 2007	10.17190/AMF/1245984
US-WCr	willowcreek	DBF	-90.08	45.81	4.0	787	5.4	23.2	Yes/Yes	Cook et al, 2004	10.17190/AMF/1246111
US-Whs	luckyhills	OSH	-110.05	31.74	17.6	320	0.5	0.5	Yes/Yes	Scott et al., 2015	10.17190/AMF/1246113
US-Wkg	kendall	GRA	-109.94	31.74	15.6	340	0.8	0.3	Yes/Yes	Scott et al., 2010	10.17190/AMF/1246112
US-Wrc	windriver	ENF	-121.95	45.82	8.8	2452	8.7	60.0	No/No	Wharton et al., 2012	10.17190/AMF/1246114

2.3 PhenoCam data

To capture vegetation phenology, we used the V2.0 PhenoCam public data release (Milliman et al., 2019; Seyednasrollah et al., 2019a; Seyednasrollah et al., 2019b). Here, we only provide a brief overview of PhenoCam data; a full description is presented in Richardson et al. (2018) and Seyednasrollah et al. (2019b). The PhenoCam network uses high-frequency imagery from digital cameras to track vegetation phenology. Following a standard protocol, cameras are mounted overlooking the vegetation of interest, and three-channel RGB images were recorded multiple times per day (typically every 30 minutes). For each site, a region-of-interest (ROI) in the image field-of-view is delineated to focus on the canopy. Using all pixels in this ROI, statistics summarizing RGB digital numbers (DN) are generated to quantify relative changes in canopy color over time. This canopy color information can be used to accurately identify phenological time series and transition dates (e.g., spring leaf emergence and fall senescence; Keenan et al., 2014). However, canopy color from PhenoCam does not explicitly measure the physical structure of the canopy (e.g., LAI or roughness). In our analysis, we used time series of the green-chromatic coordinate (G_{CC}) to measure canopy greenness and extract transition dates,

$$G_{CC} = \frac{G_{DN}}{G_{DN}+R_{DN}+B_{DN}} \quad (9)$$

Daily values of G_{CC} were calculated from all daytime images under a 1- or 3-day moving-window (Sonnentag et al., 2012). The V2.0 data release provides four G_{CC} statistics for each moving window: mean, median, 75th percentile, and 90th percentile. In this analysis, we used the statistic that minimizes the root mean squared error (RMSE) between daily G_{CC} values and a locally weighted regression smoother (loess) at each site. The smoothing span for the loess was determined by minimizing a Bayesian Information Criterion (BIC) (Richardson et al., 2018), and the smoothed loess values are further used to identify phenological transition dates. In our

analysis, we used the 3-day moving window substantial to visualize seasonal patterns in greenness and the 1-day product to estimate transition dates. This was necessary as transition dates could not be identified in some of the dryland sites using the 3-day product. For this study, we used the start-of-season green-up date (i.e., "green-up") as our primary measure of spring phenology, as it characterizes the date of leaf emergence and acts as a clear separator between dormant and growing seasons. Specifically, this green-up date was equated to the day when 10% of the total seasonal amplitude in G_{CC} was reached. For evergreen needleleaf sites, changes in G_{CC} are caused by changes in foliage pigments on seasonal time scales, and are not related to changes in leaf area (Bowling et al., 2018; Seyednasrollah et al., 2021). The V2.0 release has been screened to remove low-quality imagery and image masks have been adjusted to account for camera field-of-view shifts. Only cameras set to fixed white balance were included, to remove negative impacts from auto-white balancing under default camera settings (Seyednasrollah et al., 2019b). Finally, we also conducted a brief supplementary comparison between G_{cc} time series and flux-tower derived estimates of broadband NDVI (e.g., Jenkins et al., 2007). We found strong similarities between these time series, indicating that PhenoCam G_{cc} can capture seasonal changes in vegetation that are also captured by radiometric measurements that are conducted at some sites. Details on these comparisons are provided in Appendix S1 and Fig. S2. Additional metadata information for each PhenoCam site, as well as example imagery and maps of vegetation cover, can be found in Table S1 and Fig. S3.

2.4 Estimating seasonal variation in aerodynamic resistance

We quantified R_{ah}, as well as the underlying components R_{am}, R_{bh}, and kB^{-1}, at a 3-day timestep to effectively visualize and identify potential seasonal patterns in these aerodynamic resistance terms among different ecosystems. First, we calculated R_{am} at a half-hour timescale using Eqn. 3.

292 Second, we used Eqns. 1 and 2 and our predictions of R_{am} to estimate a single value of kB^{-1} that
293 minimized prediction error of H across all half-hour values every three days. This value of kB^{-1}
294 at a 3-day timestep allowed R_{bh} to be calculated using Eqn. 7. Finally, we smoothed the time
295 series for each variable using a loess curve. The span for the loess curve for each variable and
296 site was optimized by minimizing the BIC, and this was the same method used for smoothing
297 PhenoCam greenness data (see Section 2.3). By smoothing over a time series of non-overlapping
298 3-day estimates, our approach captures shifts occurring during phenological transitions, even
299 under a short time duration. We chose a 3-day time scale for this averaging and subsequent
300 smoothing because it was consistent with the time scale used with PhenoCam. We note that our
301 method of estimating R_{bh} as a residual of R_{ah} and R_{am} will result in errors in H will be
302 propagating into estimates of R_{bh} and kB^{-1}. Errors in H could be derived from multiple sources,
303 but are not likely a major concern. For example, it is possible that lack of energy balance closure
304 could influence our results, especially if there is strong seasonality in the amount of closure
305 occurring in concert with seasonal changes in the Bowen ratio. However, at the handful of sites
306 where we examined this in detail, we found no evidence of strong seasonality in mid-day energy
307 balance closure, and no emerging patterns that would allow us to link poor energy balance
308 closure to strong seasonal variation in R_{bh}. Furthermore, while random or systematic
309 measurement errors in H data could influence estimates of R_{bh}, our filtering approach was
310 designed to minimize the impact of systematic errors (see section 2.2) and by averaging mid-day
311 fluxes over three days, the magnitude of random errors is also greatly reduced (e.g., Hagen et al.,
312 2006; Hollinger and Richardson, 2005).
313 Any variable exhibiting strong seasonal variability will inherently have cyclical peaks and
314 valleys. Here, we identified the timing of peaks and valleys for both R_{ah} and kB^{-1} (hereafter

315 referred to as periods characterized by either "maximum" or "minimum" values, respectively).
316 These maximum and minimum periods were then related to green-up. To do this, we first
317 computed the 25th or 75th percentiles of the whole time series for each variable at each site. We
318 then identified the days-of-year where each variable occurred above or below these 75th and 25th
319 percentiles, equating these days to the timing of seasonal maximum and minimum values,
320 respectively. The start-, middle-, and end-point for each maximum and minimum time period
321 was identified by the 10th, 50th, and 90th percentiles across these day-of-year values. To calculate
322 these relative day-of-year statistics, we used directional statistics using the *'circular'* package in
323 R (Agostinelli and Lund, 2017). To visualize and compare the timing of seasonal transitions in
324 R_{ah} and kB^{-1}, we plotted the transition dates for each of these variables against each other, as well
325 as green-up date. The transition dates for R_{ah} and kB^{-1} used for this visualization were the "end"
326 points (i.e., 90th percentile) of the distribution for timing maximum R_{ah} and kB^{-1} values (e.g., see
327 Figs. 3 and 5). We used these values as transition dates since they are representative of the
328 timing of when R_{ah} or kB^{-1} begins to decrease.
329 kB^{-1} is also frequently modeled as a response to the Reynolds roughness number (Re_*)
330 (Rigden et al., 2018), where Re_* is defined as:
331 $$Re_* = \frac{z_{0m} u_*}{\nu} \quad (10)$$
332 Here, ν is the kinematic viscosity (Massman, 1999). Thus, we plotted kB^{-1} against Re_* for each
333 season (dormant and growing) to visualize and compare our results more easily to past studies.
334 For this simple visualization, we identified the growing season as those dates between the 50%
335 green-up threshold and 50% green-down threshold (Richardson et al., 2018). The dormant
336 season was identified as the period prior to green-up.

2.5 Attribution analysis

We can attribute variability in R_{ah} to either R_{am} or R_{bh} (i.e., $R_{ah} = R_{am} + R_{bh}$; Eqn. 2), and understanding which of these factors has a stronger correspondence would provide key information to infer the primary drivers of R_{ah}. To conduct an attribution analysis, we used statistical properties defining the variance of the sum of two random variables (Rice, 2007),

$$Var(X + Y) = Var(X) + Var(Y) + 2Cov(X, Y) \quad (11)$$

Here, *Var* and *Cov* are the variance and covariance functions, respectively. We used Eqn. 11 in combination with the relationship in Eqn. 2 to attribute the relative contribution of total variance of R_{ah} or the covarying relationship between R_{am} and R_{bh},

$$Var(R_{ah}) = Var(R_{am} + R_{bh})$$

$$Var(R_{ah}) = Var(R_{am}) + Var(R_{bh}) + 2Cov(R_{am}, R_{bh}) \quad (12)$$

Calculations assumed N-1 degrees of freedom, with N being the number of independent 3-day periods. This analysis was done separately for each site using the unsmoothed time series.

2.6 Quantifying seasonal changes in roughness parameters

Seasonal shifts in kB^{-1} must be in response to either z_{0m} or z_{0h}. To help diagnose whether changes in kB^{-1} are responding to z_{0m} or z_{0h}, we quantified z_{0m} by estimating aerodynamic canopy height (h_a) at a 3-day timestep. For example, if kB^{-1} decreases even while z_{0m} increases, we can infer that changes in z_{0h} are likely having a stronger influence on kB^{-1} (e.g., Fig. 1). z_{0m} is most commonly prescribed as simple functions of mean canopy height (h_c) (e.g., $z_{0m} = 0.1h_c$), with measured canopy heights reported by site PIs. However, z_{0m} has been shown to vary significantly with leaf area (Yang and Friedl, 2003), indicating physical h_c measurements may be limited at capturing seasonal changes in z_{0m}. Aerodynamic canopy height (h_a) offers an alternative to using

observed h_c. Specifically, aerodynamic canopy height can be estimated using the Monin-Obukhov similarity theory definition of the log-wind profile,

$$u(z) = \frac{u_*}{k}\left[\ln\left(\frac{z-d}{z_{0m}}\right) - \psi_m\right] \quad (13)$$

Here, $u(z)$ is wind speed at height z, d is the zero-plane displacement height, and ψ_m is a stability function for momentum (Dyer and Hicks, 1970). Under near-neutral atmospheric stability (i.e., $\psi_m \approx 0$), Eqn. 13 can be re-arranged to determine a single value of h_a that best predicts flux-tower measurements of $\frac{ku(z)}{u_*}$ using the assumptions that $d = 0.7h_a$ and $z_{0m} = 0.1h_a$,

$$\frac{ku(z)}{u_*} = \ln\left(\frac{z-0.7h_a}{0.1h_a}\right) \quad (14)$$

While $d/z_{0m} = 7$ is a common assumption (Bonan, 2016), this ratio has been demonstrated to change with land-cover type, LAI, and stand density (Nakai et al., 2008). However, we maintained this assumption for our analysis, as we were primarily interested in simply understanding how h_a (and hence z_{0m}) changes seasonally; thus, the absolute accuracy of our h_a estimates was not critical.

To quantify seasonal variability in h_a, we first split up the time series at each site into non-overlapping 3-day windows. Within each window, a single value of h_a was optimized to minimize the mean absolute error between all observed and predicted half-hour values of $\frac{ku(z_r)}{u_*}$. This gave us one estimate of h_a every three days. For this optimization, we used a different data filtering approach than in Section 2.2. Here, we closely followed Pennypacker and Baldocchi (2016) and Chu et al. (2018). Additionally, we filtered for atmospheric neutrality, and this was the only part of our analysis to include this filter. In estimating h_a, we applied a roughness sublayer correction at forest sites (Chu et al., 2018). If the reference height (z_r) was less than

380 $1.5h_c$ (h_c equal to PI reported canopy height), we included a roughness-sublayer correction factor
381 (λ_{rs}), optimizing using the following instead of Eqn. 14:

382 $$\frac{ku(z)}{u_*} = \ln\left(\frac{z-0.7h_a}{0.1h_a}\right) + \ln(\lambda_{rs}) \quad (15)$$

383 From Chu et al. (2018), λ_{rs} = 1.25. We did not include a roughness sublayer correction in any
384 other part of our analysis, and we believe this would not meaningfully impact our results as Hu et
385 al. (2020) found that including a roughness-sublayer correction did not improve predictions of
386 turbulent fluxes. Seasonal summaries for h_a for each site are provided in Fig. S4.

387 In addition to calculating h_a, we also used wind-profile data from sites recording wind speed
388 at multiple heights to individually estimate d and z_{0m}, independent of assumptions related to
389 canopy height such as $z_{0m} = 0.1h_c$ (sites with profile data availability are listed in Table 1).
390 Specifically, we chose three sites for this analysis: US-MMS, US-Syv, and US-Ne1. We chose
391 sites for this analysis based on whether d was likely to have significant influence and on the
392 availability of relatively complete and suitable time series of wind speed at two heights. To
393 conduct this analysis, we used the difference between wind speeds at two different heights under
394 near-neutral stability to find a single value of d that best predicts the left-hand side of Eqn. 13
395 (Monteith and Unsworth, 2008):

396 $$\frac{k(u_1-u_2)}{u_*} = \log\left(\frac{z_1-d}{z_2-d}\right) \quad (16)$$

397 Here, subscripts refer to two different measurement heights, with $z_1 > z_2$. Using this estimate of
398 d, we were able to invert Eqn. 10 to obtain an estimate of z_{0m}:

399 $$z_{0m} = \frac{z-d}{\exp\left\{\frac{ku(z)}{u_*}\right\}} \quad (17)$$

2.7 Seasonal sensitivity to estimating H

While initial results indicated there was significant seasonality in both R_{ah} and kB^{-1} (Figs. 2, 3, 6), it is also common to assume $kB^{-1} = 0$ or kB^{-1} is equal to a constant value (i.e., $kB^{-1} = c$) when predicting H. To understand the implications of using either of these assumption for predicting seasonal patterns in H, we calculated the relative difference between estimated ($\hat{H}$) and measured values of H (i.e., $\hat{H}/H$). The constant value c for each PFT was obtained from Rigden et al. (2018), and is representative of mean growing season kB^{-1}. The impacts of each assumption were evaluated by visualizing time series of the relative difference between measured and estimated H at a 3-day timestep.

3. Results

3.1 Seasonal variability in aerodynamic resistance

There were significant seasonal patterns in R_{ah} at most of our study sites, which spanned a continental-scale precipitation gradient (Fig. 2). In general, PFTs that exhibited the largest seasonal changes in leaf area (i.e., deciduous broadleaf, grassland, croplands) consistently produced strong seasonal signals in R_{ah} (Fig. 2). For example, at the wettest grassland site, a restored prairie landscape in the upper Midwest (US-Ro4, MAP = 879 mm; Markland, 2019), R_{ah} ranged from 44 s m^{-1} in the dormant season to 21 s m^{-1} in the growing season (Fig. 2). Likewise, at our driest grassland site, Kendall grassland in the Walnut Gulch Experimental Watershed of southern Arizona (US-Wkg, MAP = 340 mm; Scott et al., 2010), R_{ah} ranged from 75 s m^{-1} to 55 s m^{-1} (Fig. 2).

We further evaluated seasonal patterns by identifying the periods of the year when R_{ah} values were characteristically lower (i.e., at a "minimum") or higher (i.e., at a "maximum"). Through quantifying these timing, we found that in many cases maximum and minimum R_{ah} values occurred in distinct and non-overlapping periods, indicating distinct seasonality (Fig. 3). Specifically, we found that maximum R_{ah} occurred prior to or during green-up, while minimum R_{ah} occurred after green-up at most deciduous broadleaf forests, grasslands, shrublands, and agricultural sites (Figs. 2, 3, and S6). For example, at a set of three agricultural sites at the University of Nebraska Agricultural Research and Development Center (US-Ne1, US-Ne2, and US-Ne3; Suyker and Verma, 2010; Suyker and Verma, 2012), we found that maximum R_{ah} occurred from 120 days prior to green-up through 13 days after green-up for corn (*Zea mays* L.), while minimum R_{ah} ranged from 66 to 141 days after green-up. Similarly, for soybean (*Glycine*

max [L.] Merr.), maximum R_{ah} ranged from 197 days prior to green-up through 8 days after green-up (Fig. S5).

We also observed seasonality in R_{ah} among some, but not all, evergreen-needleleaf and woody savanna sites. Wetter evergreen and savanna sites, as measured by mean annual precipitation (Table 1), displayed little seasonal variability in R_{ah}, while drier evergreen and savanna sites with lower stand density had some of the strongest seasonal patterns in R_{ah}. For example, US-Ho1 (MAP = 1070 mm), a sub-boreal, closed canopy site in Maine with little annual needle turnover (Hollinger et al., 1999), exhibited little seasonal variation in R_{ah}, R_{am}, or R_{bh} (Fig. 2), and R_{ah} had a seasonal amplitude of only 4 s m^{-1}. In comparison, at the lower stand density Metolius young burn site in central Oregon (US-Me6, MAP = 494 mm; Ruehr et al., 2014) or the Pinyon-Juniper woody savanna site in central New Mexico (US-Mpj, MAP = 385 mm; Anderson-Teixeira et al., 2011), we observed some of the largest seasonal changes in R_{ah} among all study sites, with seasonal amplitudes of 33 and 16 s m^{-1}, respectively (Fig. 2). Furthermore, the timing of minimum and maximum R_{ah} values at these drier evergreen needleleaf and savanna sites was opposite to the patterns found at deciduous broadleaf forests, with maximum R_{ah} occurring during the growing season and minimum values more prevalent during the dormant season prior to green-up (Figs. 2, 3, and S6).

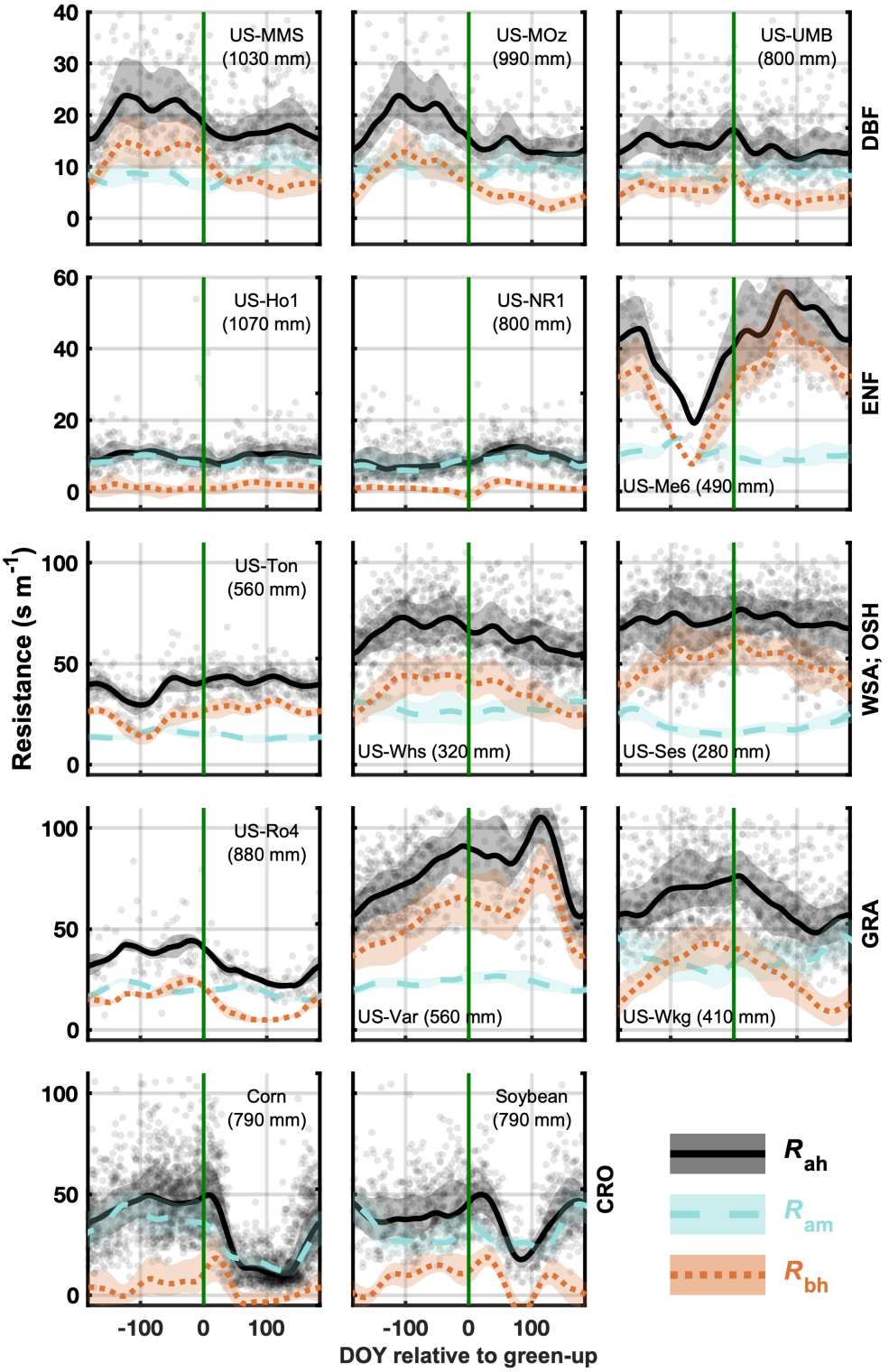

Figure 2. Seasonal changes in R_{ah}, R_{am}, and R_{bh} from example sites for each PFT. For each site, the median is calculated for each DOY across all years, and these statistics are then smoothed using a loess smoother. Confidence bounds represent the interquartile range across all years as well (25^{th}-75^{th} percentiles). Mean annual precipitation is in parentheses. The plotted points are the unsmoothed data for R_{ah}. Plots for additional sites can be found in Fig. S4.

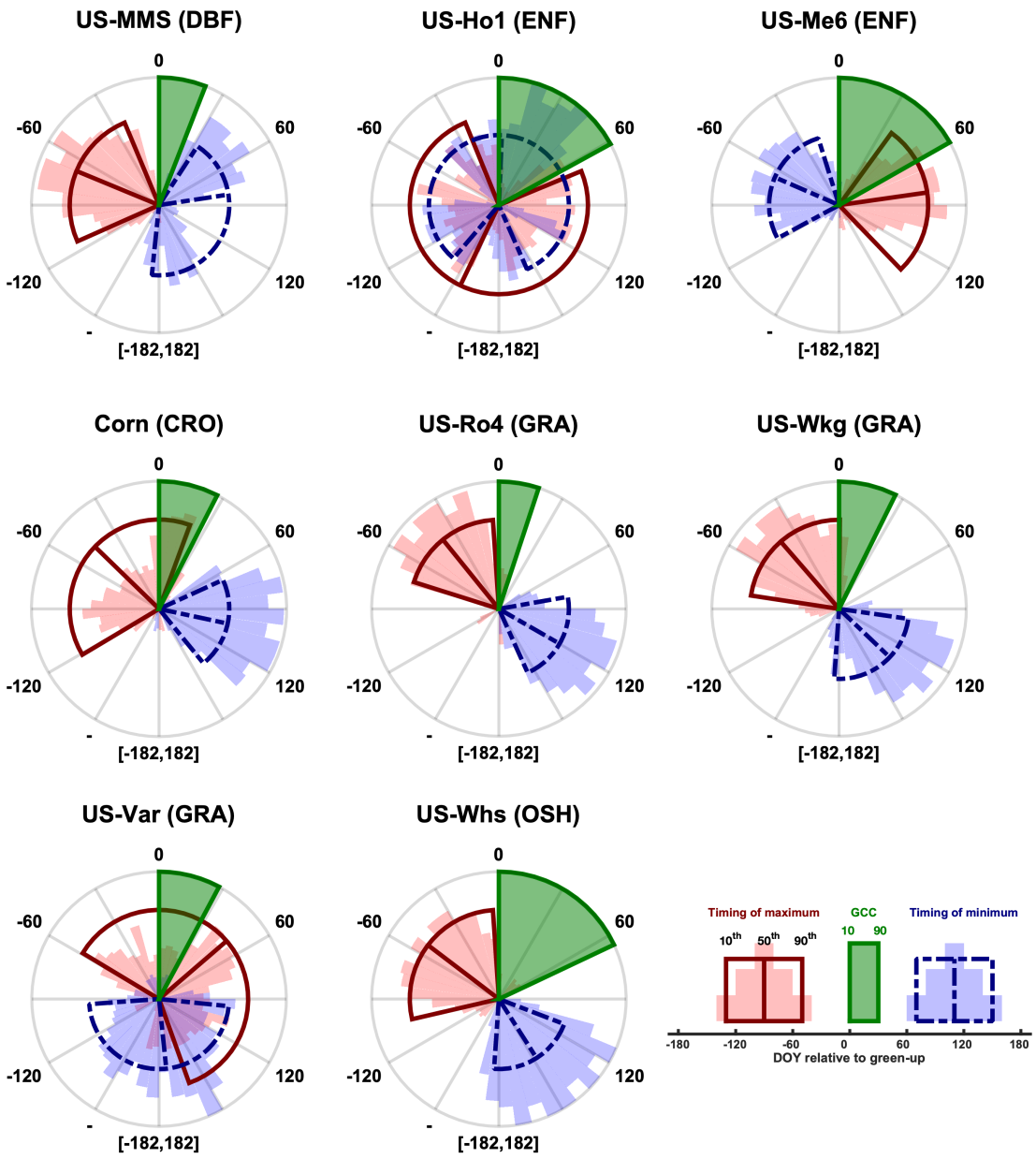

Figure 3. Timing of seasonal maximum and minimum values for aerodynamic resistance to heat transfer (R_{ah}). Red and blue histograms display the empirical distribution of the seasonal maximum or minimum timing, respectively. Specifically, the histograms are for day of year values (relative to green-up) for all days that were either above the 75th percentile (i.e. maximum) or below the 25th percentile (minimum). Day 0 (at the top of each plot) represents green-up. These empirical distributions of maximum or minimum timings are summarized by the 10th, 50th, and 90th percentiles of these relative day-of-year values as the beginning, middle, and end points, respectively (i.e., the red and blue "slices"). The green "slices" represent the green-up phenological transition period, bounded by dates when the G_{CC} curve reaches 10% and 90% of the total seasonal amplitude of G_{CC}. Plots for additional sites can be found in Fig. S6.

3.2 Inferred drivers of R_{ah} seasonality and linkages to spring phenology

Our findings suggested that seasonal variability in R_{ah} was primarily attributable to changes in R_{bh}, not R_{am}, at most of our study sites. In general, there was strong correlation in the seasonal patterns of R_{ah} and R_{bh}, but much lower correspondence between R_{ah} and R_{am} (Fig. 2). For example, at US-MMS, a 90-100 year old deciduous broadleaf forest in southern Indiana (Dragoni et al., 2011), there was a well-defined decrease in R_{ah} near green-up, shifting from 23 s m^{-1} to 15 s m^{-1} (Fig. 2). This shift in R_{ah} directly tracked R_{bh}, which shifted from 15 s m^{-1} to 7 s m^{-1}. Conversely, R_{ah} was anti-correlated with R_{am} (Fig. 2). These patterns and linkages between R_{ah} and R_{bh} were reinforced by results from our attribution analysis where the total variance in R_{ah} was partitioned between R_{am}, $R_{bh,}$ and the covariance between R_{am} and R_{bh} (Fig. 4). We found clear evidence among non-agricultural PFTs that the total variance in R_{ah} was primarily explained by R_{bh}, not R_{am} (Fig. 4). For example, across all deciduous broadleaf sites, variance in R_{bh} explained 48-92% of the total variance in R_{ah} compared to R_{am} (2-36%) (Fig. 3). There were only two non-agricultural sites where we found evidence for R_{am} having higher explanatory power than R_{bh}: CA-TP4 and US-NR1 (e.g., 65% vs 38% for CA-TP4) (Fig. 4).

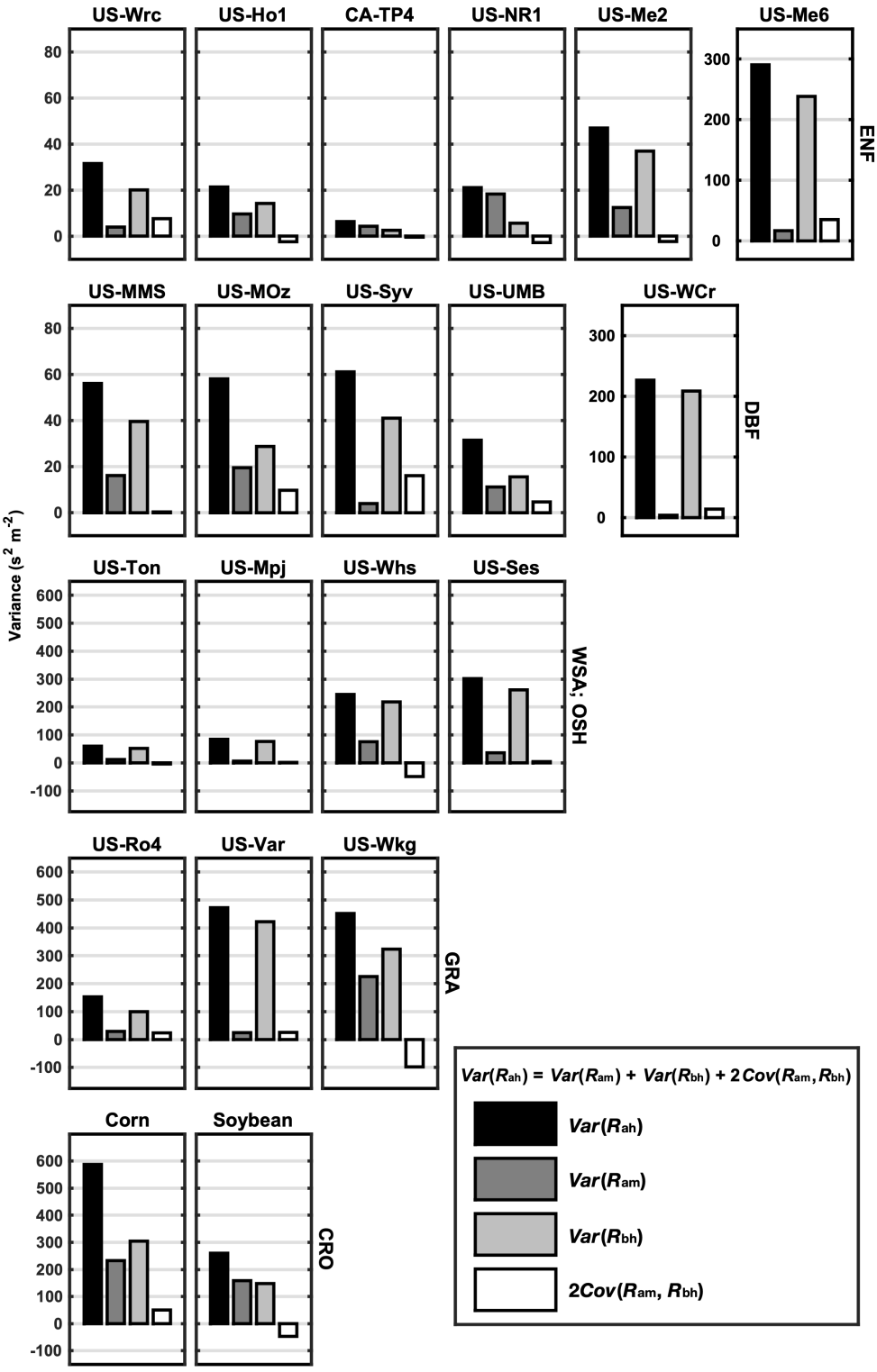

Figure 4. Attribution of the total seasonal variance in R_{ah} to either R_{am}, R_{bh}, or $2Cov$ (R_{am}, R_{bh}). Corn and soybean data are obtained from US-Ne1, US-Ne2, and US-Ne3.

Seasonal variation in R_{bh} is attributable to seasonal shifts in kB^{-1}. We found distinct and corresponding seasonal cycles between R_{bh} and kB^{-1} occurring at many sites (Figs. 2, 5, and 6); kB^{-1} generally reached its highest values immediately prior to or during green-up, followed by decreases during the transition to the growing season at deciduous broadleaf, grassland, shrubland, and agricultural sites (Figs. 5 and 6). At drier evergreen needleleaf sites, such as US-Me6, we found the opposite pattern, with kB^{-1} lower during the dormant season and increasing during the growing season (Figs. 5 and 6), with strong similarity to the signal in R_{ah} found at these same sites (Figs. 2 and 3). When comparing Figs. 3 and 5, we observe that a deciduous broadleaf site (US-MMS) the timing of maximum R_{ah} and kB^{-1} overlapped considerably. Similar patterns can be found at the other end of the precipitation gradient; at a shrubland site in southern Arizona (US-Whs), the median day-of-year of peak R_{ah} and kB^{-1} were almost identical: 43 and 45 days prior to start-of-season green-up (Figs. 3 and 5). When comparing all sites, we found a strong positive linear relationship between the transition dates for R_{ah} and kB^{-1}, with the transition dates for R_{ah} and kB^{-1} occurring within 30 days of each at 60% of all sites (Fig. 7a).

The timing of seasonal shifts in R_{ah} and kB^{-1} appeared to track green-up transition dates for some, but not all, sites (Fig. 7b,c). Linkages between green-up dates and shifts from higher to lower R_{ah} and kB^{-1} were notable at most deciduous broadleaf, grassland, and at least one shrubland site. For example, there were distinct decreases in kB^{-1} at two deciduous forest sites (US-MMS and US-MOz) immediately after spring green-up occurred, and this response was consistent even when green-up occurred approximately 30-days earlier than normal in 2012 (Fig. 6). This strong association between transition dates is visualized in Fig. 7b, c; transition dates between kB^{-1} and G_{cc} occurred within 30 days of each other for 80% of deciduous broadleaf, two out of three of grassland, and one of two of shrubland sites. By comparison, for most evergreen

needleleaf forests and woody savanna ecosystems, kB^{-1} transition dates generally occurred more than 120 days from green-up, if at all. In general, these patterns between kB^{-1} and greenness were comparable to the patterns we found for R_{ah}.

Finally, to help understand which surface roughness parameter (z_{0m} or z_{0h}) is driving kB^{-1} changes, we estimated d and z_{0m} through aerodynamic canopy height (h_a) and wind-profile data. In general, we found that h_a increases during the growing season, implying z_{0m} is also increasing (Fig. S4). We found a similar pattern for a cropland site with corn (US-Ne1), where there was a distinct increase in both d and z_{0m} during the growing season (Fig. 8). While this pattern occurred at most sites, we also found examples where z_{0m} decreased during the growing season, indicating that the canopy became smoother. Specifically, at US-MMS and US-Syv, z_{0m} decreased by approximately 1.5 m during the transition from spring to summer (Figs. 9 and S4).

3.3 R_{ah} seasonality in croplands

There were relatively unique patterns at several of the cropland sites in our analysis, compared to other sites. Specifically, a significant proportion of the variation in R_{ah} was attributable to R_{am}, contrasting with results at most other sites (Fig. 4). R_{am} exhibited significant influence at the Nebraska corn and soybean agricultural sites (US-Ne1, US-Ne2, and US-Ne3). Our attribution analysis indicated R_{am} explained a significant part of the total variance in R_{ah}, with R_{am} explaining 40% and 51% of the variability in R_{ah} for corn and soybean, respectively, compared to R_{bh} which explained 53% and 49%. This similarity can be visualized in Fig. 2, as both R_{ah} and R_{am} closely tracked each other immediately after green-up in both corn and soybean sites. Seasonal patterns in R_{bh} and kB^{-1} also differed notably compared to deciduous forest and grassland sites; R_{bh} and kB^{-1} increased immediately after green-up, followed by a sudden decrease after canopy greenness reached its seasonal maximum (Figs. 2 and 6).

Strong seasonal patterns in R_{ah} were also observed at weekly timescales at the alfalfa (*Medicago sativa* L.) sites in the Sacramento–San Joaquin River Delta in central California (US-Bi1 and US-Tw3), with R_{ah} and kB^{-1} decreasing as z_{0m} and canopy greenness increased (Figs. 9 and S7). Alfalfa harvesting takes place 5-7 times per year during the spring and summer (Hemes et al., 2019). At these two sites, we observed distinct seasonal patterns in R_{ah} responding to changes in aerodynamic canopy height (h_a), canopy greenness, and kB^{-1} (Fig. 6 and S6). At US-Bi1, changes in z_{0m} ranged from 0.02 to 0.06 m, closely tracking canopy greenness, and R_{ah} and kB^{-1} inversely tracked these changes in h_a and greenness. Similar patterns were found at US-Tw3 (Fig. S7). The data at these sites highlight three key patterns. First, kB^{-1} was the main driver of R_{ah}. Second, maximum values in R_{ah} and kB^{-1} occurred when canopy greenness and z_{0m} were at a minimum, shortly after a harvesting event. Finally, there was little-to-no change in R_{am} accompanying these patterns in R_{ah}. These results were comparable to the patterns observed in deciduous broadleaf, grassland, and shrubland sites; maximum and minimum values of R_{ah} and kB^{-1} occurred during dormant and growing periods, respectively.

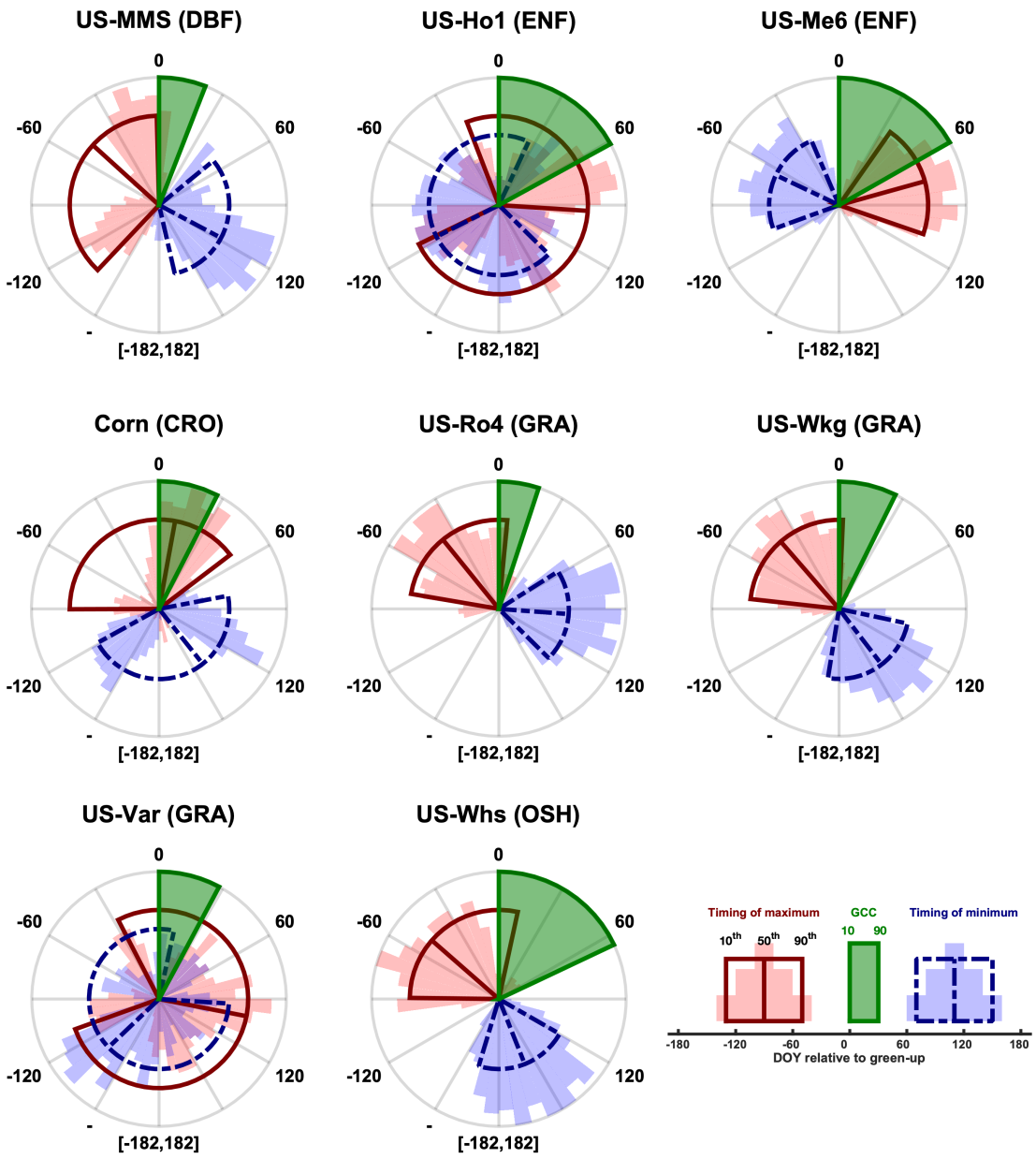

Figure. 5. Same as Fig. 3 but for kB^{-1}.

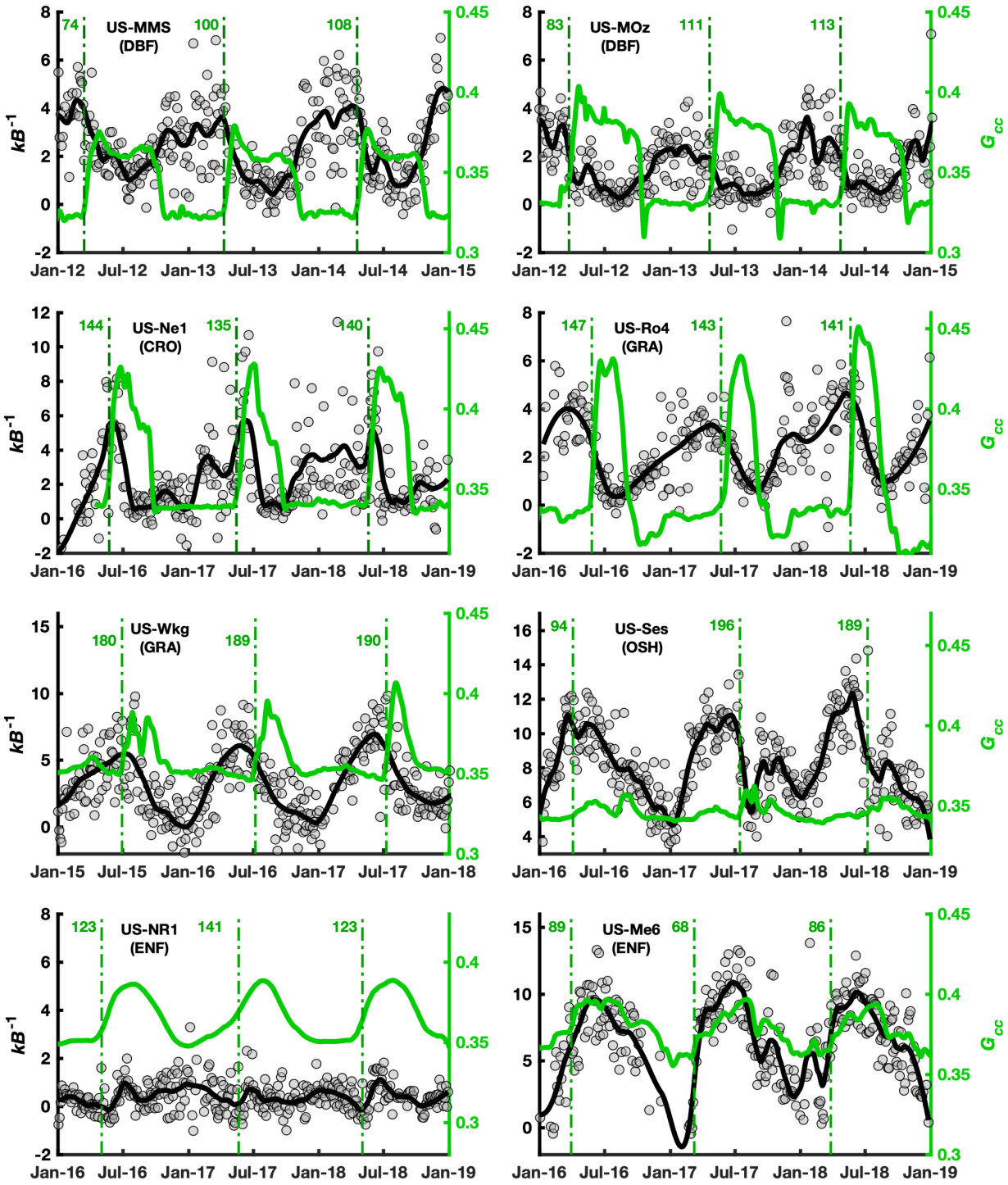

Figure 6. Time series for kB^{-1} and G_{cc} for a range of different PFTs. Each panel covers a time period of three years. Three-day optimized kB^{-1} values are represented as the grey points, while the black line indicates the smoothed time series described in Section 2.5. Solid green curves indicate PhenoCam-derived Gcc and the vertical dashed lines indicate PhenoCam transition dates for green-up. The numbers printed next to each green-up line indicates the day-of-year.

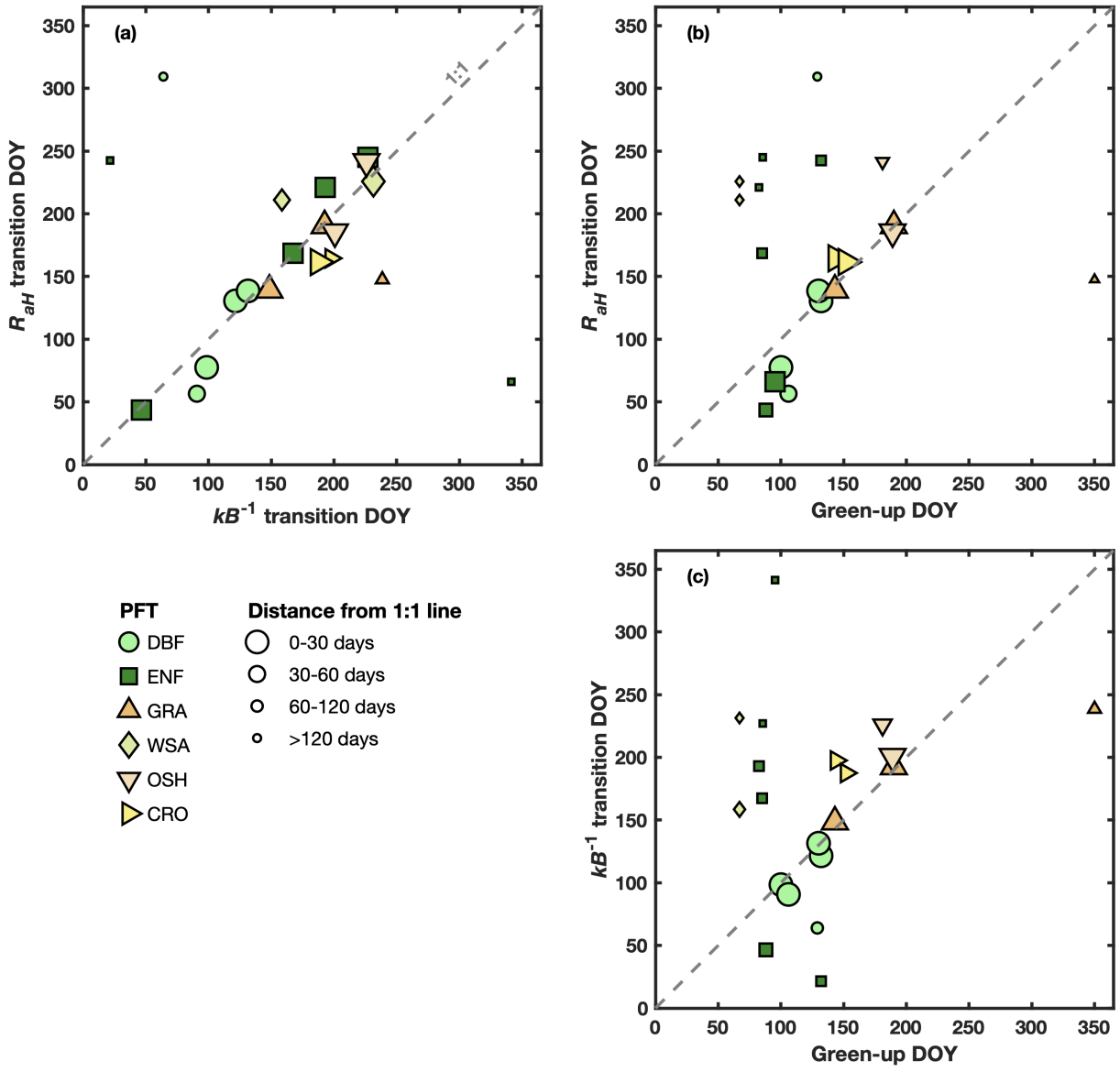

Figure 7. Comparison of transition dates for R_{ah}, kB^{-1}, and green-up. Plot symbols and colors indicate different PFTs, while the size of the plot points is inversely proportional to the distance from the 1:1 line. Transition dates for R_{ah} and kB^{-1} are equated to the end points for the empirical distribution of the timing of maximum values for each variable (e.g., see Figs. 3 and 5).

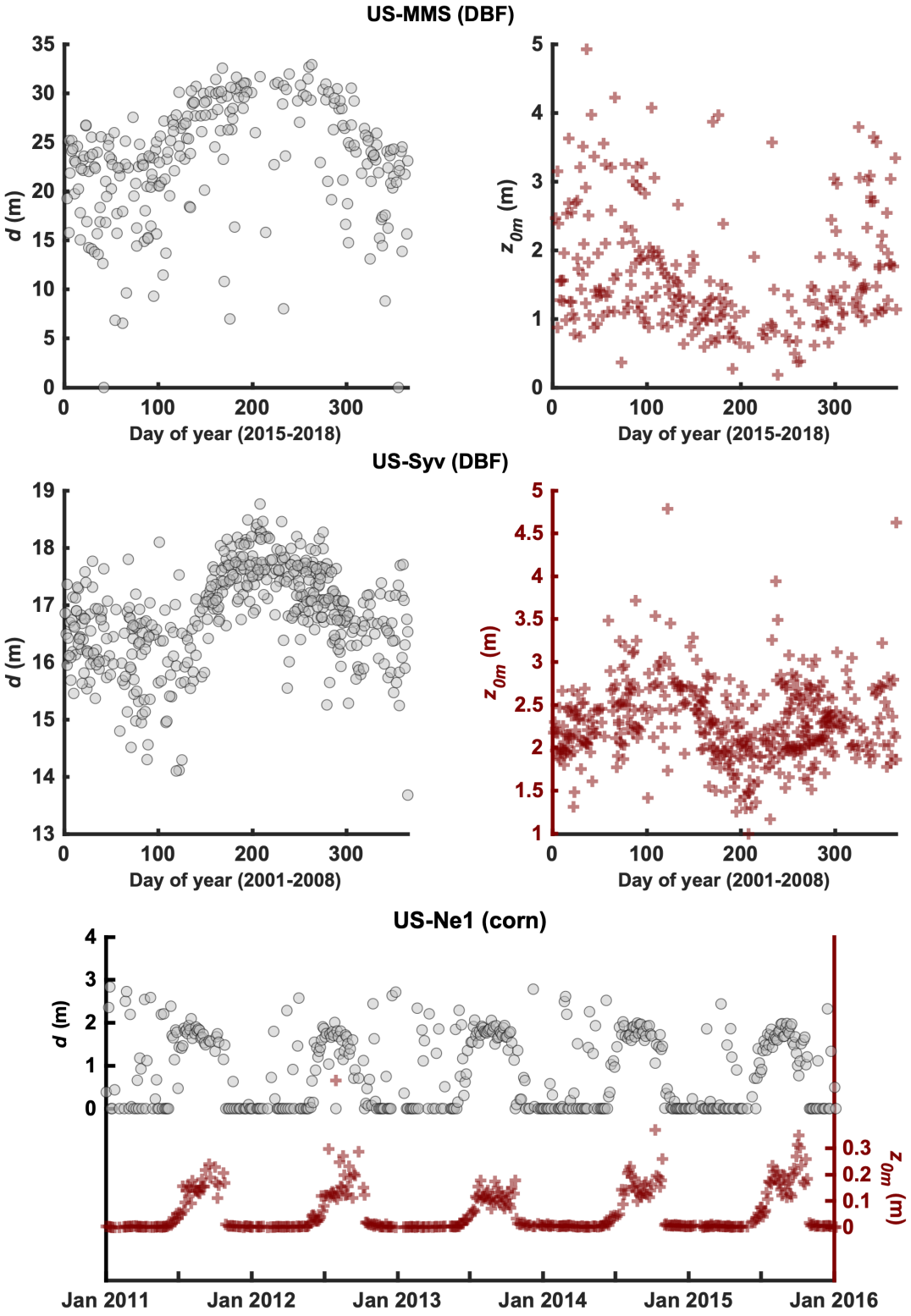

Figure 8. Changes in d and z_{0m} estimated from wind-profile data. Circles indicate estimates of d while crosses indicate estimates of z_{0m}.

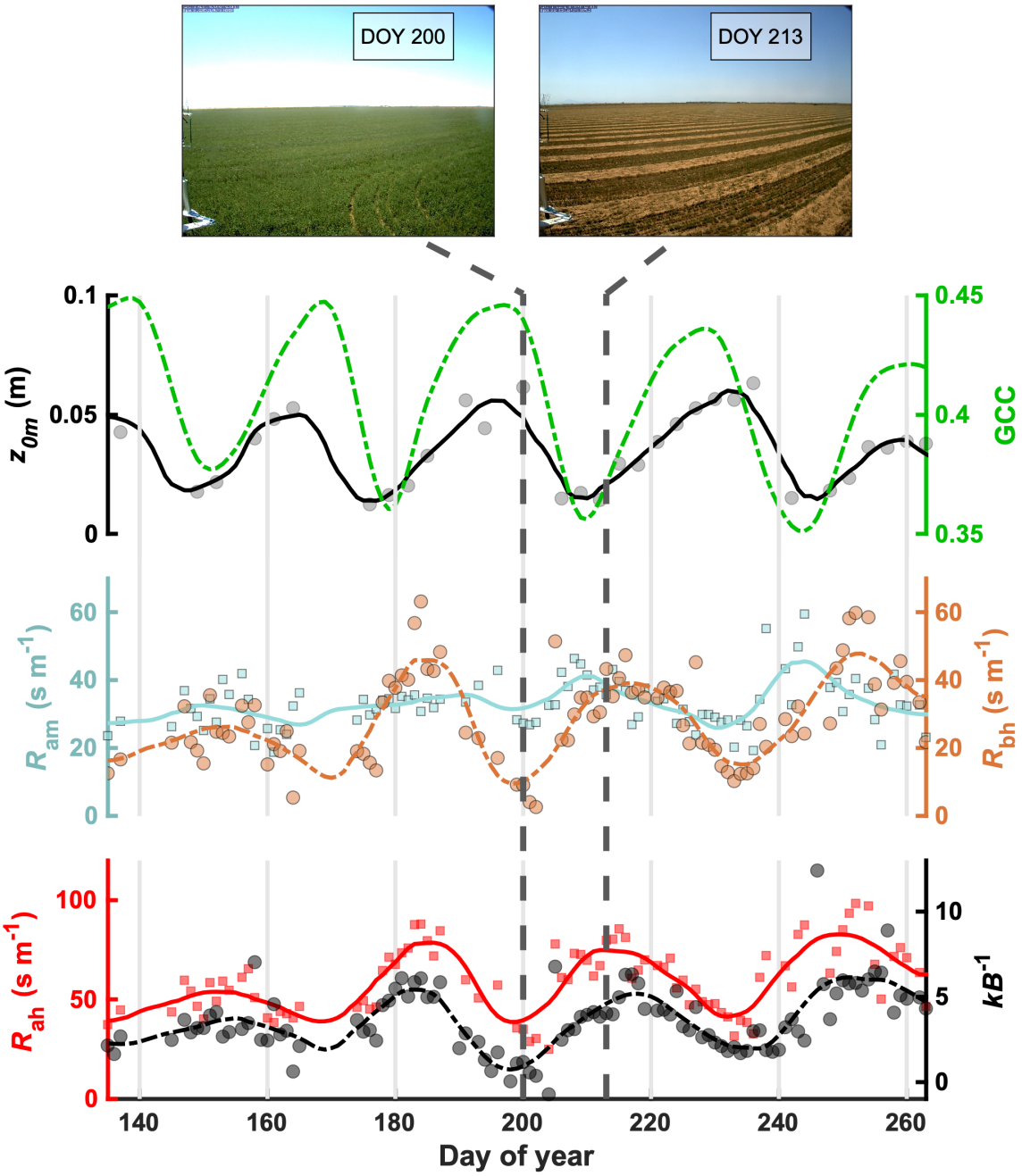

Figure 9. Growing season patterns in z_{0m} (i.e., $0.1h_a$), GCC, R_{am}, R_{bh}, R_{ah}, and kB^{-1} for an agricultural site (US-Bi1) for 2017. Images are from the PhenoCam site bouldinalfalfa at midday. Due to the short time period, these data are daily (individual points) and smoothed using a loess. Solid and dashed lines represent the smoothed values for the left and right y axes, respectively.

564 **3.4 Implications for understanding seasonal changes in aerodynamic resistance**

565 At many sites, we found evidence that kB^{-1} differs between the non-growing season and
566 growing season, indicated by the clear bifurcation in kB^{-1} with higher values occurring during the
567 non-growing season and lower values occurring during the growing season (Fig. 10). To
568 understand how this seasonal variation in kB^{-1} may influence predictions of H when compared to
569 the assumption of static kB^{-1} (i.e., $kB^{-1} = 0$ or $kB^{-1} = c$), we estimated the full annual pattern of
570 relative differences between estimated and measured H (i.e., $\hat{H}/H$) at a 3-day timestep. We found
571 that estimates of H were quite sensitive to $kB^{-1} = 0$ or $kB^{-1} = c$; at many sites, we found that the
572 highest relative differences generally occurred during the nongrowing season and under the
573 assumption $kB^{-1} = 0$ (Fig. 11). For example, at US-MMS, $\hat{H}/H$ was approximately 300% right
574 before green-up, indicating that assuming $kB^{-1} = 0$ will produced large biases (Fig. 11). At the
575 arid US-Ses shrubland site, the highest values of $\hat{H}/H$ (> 400%) occurred immediately prior to
576 green-up (Fig. 11). We found similar seasonal patterns of $\hat{H}/H$ by assuming kB^{-1} is constant for
577 each PFT (i.e., $kB^{-1} = c$), although the magnitude of $\hat{H}/H$ was considerably reduced relative to
578 $kB^{-1} = 0$ (Fig. 11). Furthermore, the seasonal patterns in $\hat{H}/H$ observed at many sites were similar
579 to the seasonal patterns in R_{ah} (Fig. 2). In summary, these results indicated that accounting for
580 seasonal changes in kB^{-1} is critical for significantly reducing biases and errors when predicting H
581 using a "big leaf" approach.

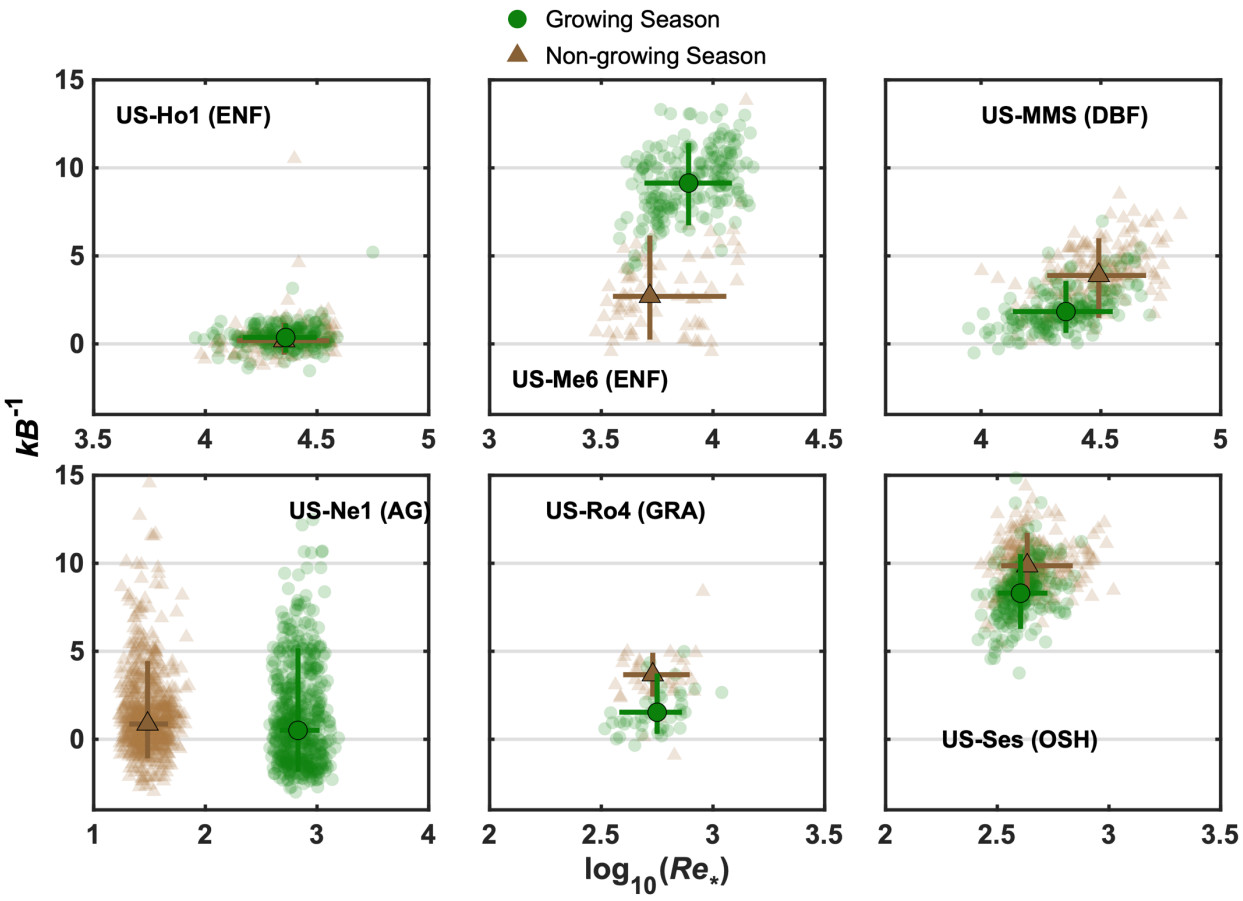

Figure 10. Relationships between kB^{-1} and the Reynolds roughness number (Re_*) for different phenology phases (non-growing and growing season) at six example sites. The darker plot points and confidence bounds represent the median and inter-quartile range of the distributions along each axis.

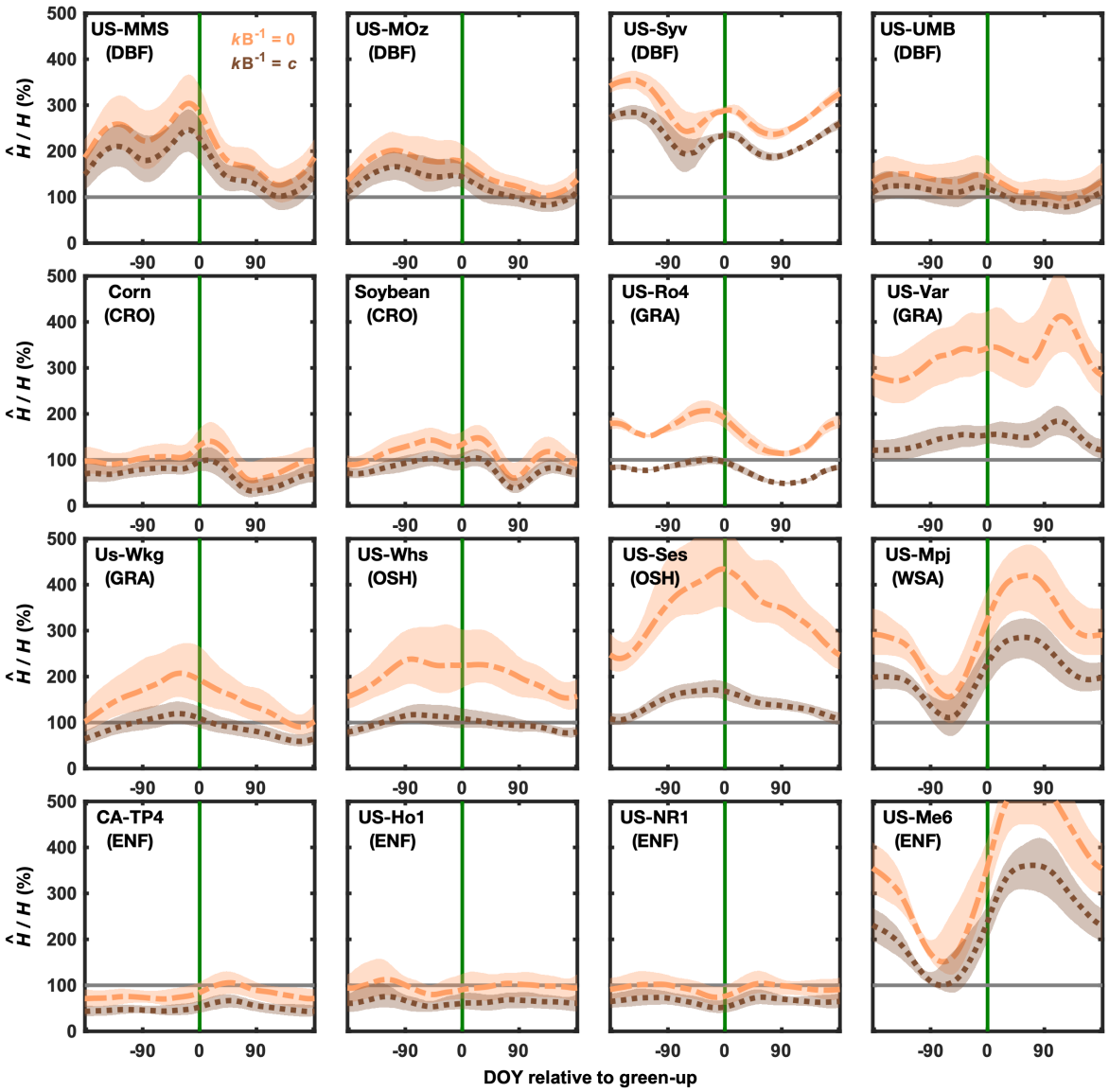

Figure 11. Seasonal signals in relative differences between measured and estimated sensible heat flux ($\hat{H}/H$) for different sites depending on whether kB^{-1} is assumed equal to 0 or a constant (i.e., $kB^{-1} = 0$ or $kB^{-1} = c$). Lines and confidence bounds are the median and interquartile range across all years.

4. Discussion

Using 190 site years of data from the AmeriFlux and PhenoCam networks, our findings highlight how aerodynamic resistance to heat transfer (R_{ah}) exhibits distinct seasonal patterns among multiple plant-functional types (PFTs) and climate regimes, and how vegetation phenology may play a role governing this seasonality in certain PFTs. Specifically, PFTs that exhibit the strongest seasonal changes in canopy structure also consistently displayed strong seasonality in R_{ah}, and the timing of the seasonal patterns in R_{ah} closely track phenological start-of-season green-up at most of these sites. Incorporating these seasonal patterns of R_{ah}, as well as potential linkages to spring phenology, is important for improving model-based predictions of sensible heat fluxes, and thus our understanding of how seasonal changes in the land surface more broadly impact atmospheric dynamics such as boundary layer height, vertical temperature profiles, and near-surface micro-climate.

4.1 How does aerodynamic resistance change seasonally?

The aerodynamic resistance to heat transfer (R_{ah}) comprises two additive resistance terms ($R_{ah} = R_{am} + R_{bh}$, Eqn. 2), and our findings provide evidence that for most sites excess resistance to heat transfer (R_{bh}) is a significantly stronger control over seasonal patterns of R_{ah}, relative to the resistance to momentum transfer (R_{am}) (Figs. 2-5). Recall that excess resistance (R_{bh}) accounts for differences between the roughness lengths for momentum (z_{0m}) and heat (z_{0h}) through the kB^{-1} parameter (i.e. $k \cdot R_{bh} \cdot u_* = \ln(z_{0m}/z_{0h}) = kB^{-1}$, Eqn. 7). In this study, we found that the seasonality (Figs. 2, 3, 5, 7a) and total variance (Fig. 4) in R_{ah} is best explained by R_{bh} and kB^{-1}. Taken together, these multiple relationships linking kB^{-1} to R_{ah} through R_{bh} imply changes in surface roughness (i.e., through z_{0m} or z_{0h}) are a key factor determining seasonal patterns in R_{ah}.

At most deciduous broadleaf, grassland, and shrubland sites, kB^{-1} decreases during start-of-season phenological transitions, implying the potential for a direct causal linkage between phenology and seasonal changes in kB^{-1} (Figs. 6, 7 and 10). Decreasing kB^{-1} in response to increasing LAI has been identified in other studies. For example, kB^{-1} is commonly modeled as a function of LAI (Brutsaert, 1979; Hu et al., 2020; Kubota and Sugita, 1994; Yang and Friedl, 2003). This modeling captures decreases of kB^{-1} in response to increasing LAI and provides accurate estimates of H as well (Qualls and Brutsaert, 1996). Decreasing kB^{-1} after green-up must be related to either z_{0m} or z_{0h} (Eqn. 6). Here, we conclude z_{0h} is more influential than z_{0m} in most cases. Specifically, we posit shifts to higher z_{0h} (lower kB^{-1}) during start-of-season green-up are due to decreases in the fractional coverage of understory and bare soil. Landscapes dominated by bare soil or sparse vegetation exhibit z_{0h} heights effectively at the soil surface, especially during warm and dry meteorological conditions where the soil is acting the primary source of heat (Verhoef et al., 1997; Yang et al., 2008). A theoretical addition of taller un-foliated roughness elements to a landscape would increase z_{0m}, while z_{0h} would remain unchanged due to surface temperature of the understory exceeding that of the canopy temperature (Brutsaert and Sugita, 1996). During phenological transitions, such as leaf emergence in temperate deciduous forests, the canopy fills in, the coverage of bare soil and understory decreases, and transpiration increases cooling of the surface (Verhoef et al., 1997), together leading to increases in z_{0h} and lowering kB^{-1}. Similar behavior of kB^{-1} is found between PFTs that have dense and sparse canopies. Permeable-rough surfaces (e.g., deciduous broadleaf or agriculture sties) have kB^{-1} values lower than bluff-rough surfaces (e.g. shrubland sites) (Brutsaert, 1982; Rigden et al., 2018). These bluff-rough surfaces, generally occurring at more arid sites, have higher proportions of land cover dominated by bare soil (Fig. S3).

636 While changes in z_{0m}, as well as z_{0h}, may also play a role in altering kB^{-1}, our results imply
637 that observed changes in z_{0m} are not driving seasonal decreases in kB^{-1}. Specifically, we found
638 that z_{0m} generally increases during the growing season, indicated by increasing aerodynamic
639 canopy height (h_a; Fig. S4) or wind-profile data (Fig. 8). All other factors being equal, increasing
640 z_{0m} by itself would lead to higher kB^{-1}; however, we found that kB^{1} decreases after green-up
641 (Figs. 5, 6, and 9). Therefore, we infer that increases in z_{0h} offset increasing z_{0m}, thereby leading
642 to decreases in kB^{-1} (e.g., Fig. 1) and implying z_{0h} is the more important control over kB^{-1}.
643 Patterns observed at an alfalfa agricultural site (US-Bi1, Fig. 8) capture this dynamic. Significant
644 decreases in z_{0m} after a harvesting event by itself should lead to decreasing kB^{-1}. However, we
645 found kB^{-1} increases after harvesting events, likely due to significant decrease in z_{0h} relative to
646 z_{0m}. Increases in z_{0m} after green-up, while common, are not ubiquitous. Decreases in z_{0m} can also
647 occur. Specifically, functions relating z_{0m} to the plant area index (i.e. PAI) exhibit non-monotonic
648 relationship and higher leaf area and foliage density at the top of the canopy can act as a smooth
649 surface (Blanken and Black, 2004; Shaw and Pereira, 1982). While we see such decreases in z_{0m}
650 at US-MMS, US-Syv, and US-NR1 (Figs. 8 and S4), this likely does not outweigh the
651 importance of z_{0h} given its strong influence at other sites.
652 While z_{0h} may have more control over seasonal changes in R_{ah} relative to z_{0m}, this is partially
653 due to z_{0m} simply not changing as much relative to z_{0h} between the non-growing and growing
654 seasons, as the physical structure of the canopy generally remains in place even if it is defoliated
655 (Nakai et al., 2008). Using the corn and soybean sites, we can investigate and better understand
656 the influence of z_{0m} in a system where the landscape transforms from bare soil to a full canopy
657 within a season. Here, we found patterns in R_{am} closely tracking R_{ah} (Fig. 2), and R_{am} explains
658 significantly more of the observed variance in R_{ah} compared to other sites (Fig. 4). This increased

659 importance in R_{am} is due to significant increases in z_{0m} as the crops increase in height (Figs. 2 and
660 8) and the subsequent effect on the log-wind profile (Eqn. 10).
661 Phenology does not have the same level of control over R_{ah} in evergreen-needleleaf sites
662 (Figs. 2, 3 and 5). This is not surprising, given that our evergreen-needleleaf sites exhibit only
663 minor leaf turnover each season. Where we did observe seasonal changes in R_{ah} (e.g., US-Me6),
664 these changes are also associated with changes in R_{bh} and kB^{-1}, comparable to other PFTs.
665 Therefore, changes in R_{ah} in evergreen-needleleaf sites are not driven by changing leaf area and
666 the fractional cover of the forest canopy, but likely by two other interacting factors. First,
667 increasing solar radiation and surface heating during the course of the growing season alters the
668 temperature source height (z_{0h}), thereby altering R_{ah} through kB^{-1}, comparable to diurnal changes
669 in kB^{-1} tracking solar radiation (Fig. 1) (Lhomme et al., 1997; Yang et al., 2008). Second, these
670 impacts of seasonal changes in solar radiation on kB^{-1} only occur at more arid sites with taller
671 vegetation, compared to shrublands or grasslands, and that likely have lower stand density (i.e.,
672 US-Me2, US-Me6, and US-Mpj; Figs. 2 and S2). The higher exposure of the understory or bare
673 soil, compared to the more closed canopy sites (i.e., CA-TP4, US-Ho1, US-NR1), exacerbates
674 the effects these changing environmental conditions have on kB^{-1}. Finally, it should be noted that
675 phenology may still play an important role in controlling seasonal patterns of kB^{-1} at lower
676 density evergreen-needleleaf sites through the phenology of understory vegetation. However, the
677 greenness index from PhenoCam for these sites is only derived for the canopy and does not
678 capture the understory phenology.
679 In this analysis, we highlight phenology may be a key driver over observed seasonal shifts
680 in kB^{-1} in some ecosystems, which subsequently impacts R_{ah} and predictions of H. However, the
681 full seasonal trajectory of kB^{-1} is not explained by phenology alone; across the sites we

682 considered, significant variations in R_{bh} and kB^{-1} occurred well before and after phenological
683 transitions (Figs. 2 and 6). For example, at a semi-arid grassland site in southern Arizona (US-
684 Wkg), we observed distinct increases in kB^{-1} beginning in January of each year, which continued
685 throughout the dormant season prior to green-up (Fig. 6). These shifts in kB^{-1} occurred well after
686 senescence and before spring green-up, and such shifts are likely influenced by other
687 environmental or meteorological factors, including evapotranspiration, net radiation, wind speed,
688 and surface temperature (e.g., Blyth and Dolman, 1995). As a brief supplementary analysis, we
689 conducted a multiple linear regression at US-Wkg that related kB^{-1} to a list of meteorological
690 factors: R_n, surface temperature (T_s), latent heat flux, soil water content, wind speed, and
691 cumulative 10-day precipitation. We found that T_s emerged as the most important among these
692 variables at seasonal time scales ($p < 0.001$, Table S2), having a strong positive relationship
693 with kB^{-1} (Fig. S8). This influence of T_s is likely due to progressively warmer soil conditions that
694 occur from January-June under increasing R_n, with the soil thereby acting as the primary source
695 of heat exchange, relative to the canopy, and resulting in z_{0h} to be at the height of the soil surface.
696 As monsoonal precipitation begins in late-June or July and green-up occurs, the soil cools and is
697 less sensitive to continued increases in R_n (Table S2). While this analysis is admittedly brief, it
698 does indicate that other factors are key for considering seasonal drivers of kB^{-1}. In general,
699 quantifying the influence of these factors on kB^{-1} – as well as how they interact with each other
700 and phenology – is crucial for developing accurate models of kB^{-1}.

701 **4.2 How does changing aerodynamic resistance influence predictions of *H*?**

702 Substantial differences between estimated ($\hat{H}$) and measured H occurred when kB^{-1} is
703 assumed constant or equal to 0 (Fig. 11). These results have important implications for modeling
704 of the land-surface energy balance using "big leaf" energy balance equations (e.g., Eqn. 1). First,

simplified assumptions of a static kB^{-1} (i.e., $kB^{-1} = 0$ or kB^{-1} is constant) are insufficient to accurately model the complete seasonal trajectory of H. Assuming $z_{0m} = z_{0h}$ (i.e., $kB^{-1} = 0$) appears to be invalid for vegetated surfaces, a result agreeing well with the literature (Yang et al., 2008). Similarly, assuming a constant value for each PFT, while helping to reduce biases (i.e., $\hat{H}/H$) relative to the assumption $kB^{-1} = 0$, still resulted in significant seasonal deviations from measured H at many sites. These results highlight that including a time-varying estimate of kB^{-1} that accounts for changes can eliminate seasonal patterns in $\hat{H}/H$ compared to assuming $kB^{-1} = 0$ or $kB^{-1} = c$, implying that anticipating how and why surface roughness changes is important for understanding seasonal dynamics in land-atmosphere interactions (Blythe and Dolman, 1994, Kustas et al., 1989).

4.3 Implications and directions for future work

The sensitivity of H to seasonal variations in kB^{-1} is unexpected when compared to inferences from past studies. Increasing z_{0m} under land-cover shifts from grasslands to aerodynamically rougher forests leads to increased turbulence and decreasing resistance, subsequently impacting surface temperature (Burakowski et al., 2018; Lee et al., 2011). Such mechanisms have been suggested to occur during phenological transitions; increases in z_{0m} during green-up could decrease aerodynamic resistance to momentum transfer (Peñuelas et al., 2009). Conversely, phenology may only play a minor role controlling aerodynamic resistance. For example, in deciduous broadleaf forests, observed increases in R_{ah} during phenological transitions have been attributed to decreasing synoptic-scale wind speed, and not z_{0m} (Moon et al., 2020). Overall, our findings provide important new insight into the role of seasonally changing roughness, which in many cases appears to be associated with phenology, as a control on H. Perhaps more consequentially, the significant seasonal biases observed under the assumption of constant kB^{-1}

implies the behavior for both z_{0m} and z_{0h} represents a key source of uncertainty for modeling land-atmosphere interactions.

Resolving uncertainty in the behavior of z_{0m} and z_{0h} at seasonal time scales is not only important for model improvement, it is critical for understanding how seasonal changes in H may impact the atmospheric dynamics, such as boundary layer height, temperature profiles, and micro-climate (Helbig et al., 2020). For example, due to the exponential nature of kB^{-1} (Eqn. 6), small increases in z_{0h} would reduce R_{ah}, leading to increased H and potentially decreasing aerodynamic surface temperature and near-surface air temperature (Novick and Katul, 2020). Understanding such dynamics will likely be important for anticipating ecosystem impacts as phenology responds to a changing climate (Richardson et al., 2013). To reduce this uncertainty, developing prognostic models of kB^{-1} as a function of different environmental factors – including phenology – is a key next step. Other studies have modeled differences in kB^{-1} among different PFTs, for example as a function of u_* or Re_* (e.g., Rigden et al., 2018). Expanding on such models to capture the seasonal shifts and bifurcation of kB^{-1} would lead to a stronger understanding of how the horizontal and vertical structure of surface roughness elements impacts H (Garratt and Hicks, 1973; Maurer et al., 2013). Finally, while more complex land-surface models such as CLM or a multi-layer approach do not rely on kB^{-1}, our work motivates the need for investigations into how seasonal changes in land-surface properties might impact predictions from these systems-based models.

Conclusions

Through a continental-scale synthesis integrating AmeriFlux and PhenoCam data and applying Monin-Obukhov similarity theory, we find that seasonal variability in aerodynamic resistance to heat transfer is pervasive across a range of ecosystems. We found evidence that the

751 mechanisms underlying this variation in aerodynamic resistance are likely linked to vegetation
752 phenology in deciduous broadleaf, grassland, agricultural, and shrublands. Specifically, shifts to
753 a larger leaf area led to z_{0h} increases during green-up, leading to decreases in kB^{-1} and in the
754 overall total aerodynamic resistance to heat transfer. By comparison, the role of changing surface
755 roughness to momentum transfer (z_{0m}) appeared to be minimal compared to z_{0h}. The total impact
756 of seasonal variation in kB^{-1} on model-based estimates of sensible-heat flux is important; large
757 biases in ($\hat{H}/H$) occurred when assuming kB^{-1} is constant. Predicting the full seasonal trajectory
758 of sensible heat flux using simple one-layer land-surface energy balance models requires
759 prognostic models and parametrizations that account for seasonal changes in kB^{-1} in response to
760 phenology and other environmental and meteorological factors. In conclusion, we found
761 evidence vegetation phenology can influence surface-roughness at relatively fine temporal
762 scales, directly impacting seasonal variability in aerodynamic resistance to heat transfer across a
763 range of North American ecosystems. Because this variation in aerodynamic resistance also
764 influences the land-surface energy balance, our findings provide insight into how
765 land-atmosphere interactions operate at seasonal time scales.

Acknowledgments

This research was supported by an NSF Macrosystems Biology award (DEB-1702697). We thank AmeriFlux site PIs John Baker, Ken Bible, Christopher Gough, Beverly Law, and Sonia Wharton for making their data publicly available. In addition, funding for AmeriFlux data resources was provided by the U.S. Department of Energy's Office of Science. Additional support was provided by the NASA Ecostress project to D. Baldocchi. We also thank our many PhenoCam site collaborators. Additional site-specific acknowledgments can be found in Table S1. All data and code used to conduct this research is publicly available on the Mendeley Data Repository (DOI: XXXXX).

References

Agostinelli, C. and Lund, U., 2017. R package 'circular': Circular Statistics (version 0.4-93). https://r-forge.r-project.org/projects/circular/

Anderson-Teixeira, K.J., Delong, J.P., Fox, A.M., Brese, D.A. and Litvak, M.E., 2011. Differential responses of production and respiration to temperature and moisture drive the carbon balance across a climatic gradient in New Mexico. Global Change Biol., 17(1): 410-424. https://doi.org/10.1111/j.1365-2486.2010.02269.x

Baldocchi, D. and Ma, S.Y., 2013. How will land use affect air temperature in the surface boundary layer? Lessons learned from a comparative study on the energy balance of an oak savanna and annual grassland in California, USA. Tellus Series B-Chemical and Physical Meteorology, 65. https://doi.org/10.3402/tellusb.v65i0.19994

Betts, A.K., 2004. Understanding hydrometeorology using global models. Bulletin of the American Meteorological Society, 85(11): 1673-+. https://doi.org/10.1175/Bams-85-11-1673

Blanken, P.D. and Black, T.A., 2004. The canopy conductance of a boreal aspen forest, Prince Albert National Park, Canada. Hydrological Processes, 18(9): 1561-1578. https://doi.org/10.1002/hyp.1406

Blyth, E.M. and Dolman, A.J., 1995. The roughness length for heat of sparse vegetation. Journal of Applied Meteorology, 34(2): 583-585. https://doi.org/10.1175/1520-0450-34.2.583

Bonan, G., 2016. Ecological Climatology: Concepts and Applications. Cambridge University Press, New York, 679 pp.

Bowling, D.R. et al., 2018. Limitations to winter and spring photosynthesis of a Rocky Mountain subalpine forest. Agr. Forest Meteorol., 252: 241-255. https://doi.org/10.1016/j.agrformet.2018.01.025

Brutsaert, W., 1979. Heat and mass-transfer to and from surfaces with dense vegetation or similar permeable roughness. Boundary-Layer Meteorology, 16(3): 365-388. https://doi.org/10.1007/Bf02220492

Brutsaert, W., 1982. Evaporation into the atmosphere: theory, history, and applications. Springer Netherlands, Netherlands, 299 pp.

Brutsaert, W. and Sugita, M., 1996. Sensible heat transfer parameterization for surfaces with anisothermal dense vegetation. Journal of the Atmospheric Sciences, 53(2): 209-216. https://doi.org/10.1175/1520-0469(1996)053<0209:Shtpfs>2.0.Co;2

Burakowski, E. et al., 2018. The role of surface roughness, albedo, and Bowen ratio on ecosystem energy balance in the Eastern United States. Agr. Forest Meteorol., 249: 367-376. https://doi.org/10.1016/j.agrformet.2017.11.030

Burns, S.P., Blanken, P.D., Turnipseed, A.A., Hu, J. and Monson, R.K., 2015. The influence of warm-season precipitation on the diel cycle of the surface energy balance and carbon dioxide at a Colorado subalpine forest site. Biogeosciences, 12(23): 7349-7377. https://doi.org/10.5194/bg-12-7349-2015

Businger, J.A., Wyngaard, J.C., Izumi, Y. and Bradley, E.F., 1971. Flux-profile relationships in the atmospheric surface layer. Journal of the Atmospheric Sciences, 28(2): 181-189. https://doi.org/10.1175/1520-0469(1971)028%3C0181:FPRITA%3E2.0.CO;2

Campbell, G.S. and Norman, J.M., 1998. An Introduction to Environmental Biophysics. Springer, New York, 286 pp.

Chu, H.S. et al., 2018. Temporal dynamics of aerodynamic canopy height derived from eddy covariance momentum flux data across North American flux networks. Geophys. Res. Lett., 45(17): 9275-9287. https://doi.org/10.1029/2018gl079306

Cook, B.D. et al., 2004. Carbon exchange and venting anomalies in an upland deciduous forest in northern Wisconsin, USA. Agr. Forest Meteorol., 126(3-4): 271-295. https://doi.org/10.1016/j.agrformet.2004.06.008

Desai, A.R., Bolstad, P.V., Cook, B.D., Davis, K.J. and Carey, E.V., 2005. Comparing net ecosystem exchange of carbon dioxide between an old-growth and mature forest in the upper Midwest, USA. Agr. Forest Meteorol., 128(1-2): 33-55. https://doi.org/10.1016/j.agrformet.2004.09.005

Dolman, A.J., 1986. Estimates of roughness length and zero plane displacement for a foliated and non-foliated oak canopy. Agr. Forest Meteorol., 36(3): 241-248. https://doi.org/10.1016/0168-1923(86)90038-9

Dragoni, D. et al., 2011. Evidence of increased net ecosystem productivity associated with a longer vegetated season in a deciduous forest in south-central Indiana, USA. Global Change Biol., 17(2): 886-897. https://doi.org/10.1111/j.1365-2486.2010.02281.x

Dyer, A.J. and Hicks, B.B., 1970. Flux-gradient relationships in constant flux layer. Quarterly Journal of the Royal Meteorological Society, 96(410): 715-+. https://doi.org/10.1002/qj.49709641012

Fitzjarrald, D.R., Acevedo, O.C. and Moore, K.E., 2001. Climatic consequences of leaf presence in the eastern United States. J. Clim., 14(4): 598-614. https://doi.org/10.1175/1520-0442(2001)014<0598:Ccolpi>2.0.Co;2

Garratt, J.R. and Francey, R.J., 1978. Bulk characteristics of heat transfer in the unstable, baroclinic atmospheric boundary layer. Boundary-Layer Meteorology, 15(4): 399-421. https://doi.org/10.1007/BF00120603

Garratt, J.R. and Hicks, B.B., 1973. Momentum, heat and water-vapor transfer to and from natural and artificial surfaces. Quarterly Journal of the Royal Meteorological Society, 99(422): 680-687. https://doi.org/10.1256/smsqj.42208

Gough, C.M. et al., 2013. Sustained carbon uptake and storage following moderate disturbance in a Great Lakes forest. Ecol. Appl., 23(5): 1202-1215. https://doi.org/10.1890/12-1554.1

Gu, L.H. et al., 2016. Testing a land model in ecosystem functional space via a comparison of observed and modeled ecosystem flux responses to precipitation regimes and associated stresses in a Central US forest. Journal of Geophysical Research-Biogeosciences, 121(7): 1884-1902. https://doi.org/10.1002/2015jg003302

Hagen, S.C. et al., 2006. Statistical uncertainty of eddy flux-based estimates of gross ecosystem carbon exchange at Howland Forest, Maine. Journal of Geophysical Research-Atmospheres, 111(D8). https://doi.org/10.1029/2005jd006154

Helbig, M. et al., 2020. Understanding land-atmosphere interactions through tower-based flux and continuous atmospheric boundary layer measurements [White paper]. https://ameriflux.lbl.gov/community/highlight/whitepaper-understanding-land-atmosphere-interactions-through-tower-based-flux-and-continuous-atmospheric-boundary-layer-measurements/

Hemes, K.S. et al., 2019. Assessing the carbon and climate benefit of restoring degraded agricultural peat soils to managed wetlands. Agr. Forest Meteorol., 268: 202-214. https://doi.org/10.1016/j.agrformet.2019.01.017

Hollinger, D.Y. et al., 1999. Seasonal patterns and environmental control of carbon dioxide and water vapour exchange in an ecotonal boreal forest. Global Change Biol., 5(8): 891-902. https://doi.org/10.1046/j.1365-2486.1999.00281.x

Hollinger, D.Y. and Richardson, A.D., 2005. Uncertainty in eddy covariance measurements and its application to physiological models. Tree Physiology, 25(7): 873-885. https://doi.org/10.1093/treephys/25.7.873

Hu, X., Shi, L., Lin, L. and Magliulo, V., 2020. Improving surface roughness lengths estimation using machine learning algorithms. Agr. Forest Meteorol., 287: 107956. https://doi.org/10.1016/j.agrformet.2020.107956

Jenkins, J.P. et al., 2007. Refining light-use efficiency calculations for a deciduous forest canopy using simultaneous tower-based carbon flux and radiometric measurements. Agr. Forest Meteorol., 143(1-2): 64-79. https://doi.org/10.1016/j.agrformet.2006.11.008

Keenan, T.F. et al., 2014. Tracking forest phenology and seasonal physiology using digital repeat photography: a critical assessment. Ecol. Appl., 24(6): 1478-1489. https://doi.org/10.1890/13-0652.1

Knauer, J., El-Madany, T.S., Zaehle, S. and Migliavacca, M., 2018. Bigleaf-An R package for the calculation of physical and physiological ecosystem properties from eddy covariance data. Plos One, 13(8). https://doi.org/10.1371/journal.pone.0201114

Kubota, A. and Sugita, M., 1994. Radiometrically determined skin temperature and scalar roughness to estimate surface heat-flux. Part I: Parameterization of radiometric scalar

roughness. Boundary-Layer Meteorology, 69(4): 397-416. https://doi.org/10.1007/Bf00718127

Kustas, W.P. et al., 1989. Determination of sensible heat-flux over sparse canopy using thermal infrared data. Agr. Forest Meteorol., 44(3-4): 197-216. https://doi.org/10.1016/0168-1923(89)90017-8

Lawrence, D. et al., 2018. Technical Description of version 5.0 of the Community Land Model (CLM).

Lee, X. et al., 2011. Observed increase in local cooling effect of deforestation at higher latitudes. Nature, 479(7373): 384-387. https://doi.org/10.1038/nature10588

Lhomme, J.P., Troufleau, D., Monteny, B., Chehbouni, A. and Bauduin, S., 1997. Sensible heat flux and radiometric surface temperature over sparse Sahelian vegetation II. A model for the kB-1 parameter. Journal of Hydrology, 188(1-4): 839-854. https://doi.org/10.1016/S0022-1694(96)03173-3

Ma, S., Baldocchi, D., Wolf, S. and Verfaillie, J., 2016. Slow ecosystem responses conditionally regulate annual carbon balance over 15 years in Californian oak-grass savanna. Agr. Forest Meteorol., 228: 252-264. https://doi.org/10.1016/j.agrformet.2016.07.016

Ma, S.Y., Baldocchi, D.D., Xu, L.K. and Hehn, T., 2007. Inter-annual variability in carbon dioxide exchange of an oak/grass savanna and open grassland in California. Agr. Forest Meteorol., 147(3-4): 157-171. https://doi.org/10.1016/j.agrformet.2007.07.008

Markland, T.C., 2019. Carbon balance and evapotranspiration rates of a restored prairie and a conventional corn/soybean rotation (M.S. Thesis). University of Minnesota - Twin Cities, Minneapolis, MN.

Massman, W.J., 1999. A model study of kB(H)(-1) for vegetated surfaces using 'localized near-field' Lagrangian theory. Journal of Hydrology, 223(1-2): 27-43. https://doi.org/10.1016/S0022-1694(99)00104-3

Maurer, K.D., Hardiman, B.S., Vogel, C.S. and Bohrer, G., 2013. Canopy-structure effects on surface roughness parameters: Observations in a Great Lakes mixed-deciduous forest. Agr. Forest Meteorol., 177: 24-34. https://doi.org/10.1016/j.agrformet.2013.04.002

Milliman, T. et al., 2019. PhenoCam Dataset v2.0: Digital camera imagery from the PhenoCam Network, 2000-2018. ORNL DAAC, Oak Ridge, Tennessee, USA. https://doi.org/10.3334/ORNLDAAC/1689

Monteith, J.L. and Unsworth, M.H., 2008. Principles of Environmental Physics. Academic Press, Amsterdam, 440 pp.

Moon, M., Li, D., Rigden, A.J. and Friedl, M.A., 2020. Modification of surface energy balance during springtime: The relative importance of biophysical and meteorological changes. Agr. Forest Meteorol., 284: 107905. https://doi.org/10.1016/j.agrformet.2020.107905

921 Nakai, T. et al., 2008. Parameterisation of aerodynamic roughness over boreal, cool- and warm-
922 temperate forests. Agr. Forest Meteorol., 148(12): 1916-1925.
923 https://doi.org/10.1016/j.agrformet.2008.03.009

924 Novick, K.A. and Katul, G.G., 2020. The duality of reforestation impacts on surface and air
925 temperature. Journal of Geophysical Research-Biogeosciences, 125(4).
926 https://doi.org/10.1029/2019jg005543

927 Oikawa, P.Y. et al., 2017. Revisiting the partitioning of net ecosystem exchange of CO2 into
928 photosynthesis and respiration with simultaneous flux measurements of (CO2)-C-13 and
929 CO2, soil respiration and a biophysical model, CANVEG. Agr. Forest Meteorol., 234:
930 149-163. https://doi.org/10.1016/j.agrformet.2016.12.016

931 Owen, P.R. and Thomson, W.R., 1963. Heat transfer across rough surfaces. Journal of Fluid
932 Mechanics, 15(3): 321-334. https://doi.org/10.1017/S0022112063000288

933 Papale, D. et al., 2006. Towards a standardized processing of Net Ecosystem Exchange measured
934 with eddy covariance technique: algorithms and uncertainty estimation. Biogeosciences,
935 3(4): 571-583. https://doi.org/10.5194/bg-3-571-2006

936 Peichl, M., Arain, M.A. and Brodeur, J.J., 2010. Age effects on carbon fluxes in temperate pine
937 forests. Agr. Forest Meteorol., 150(7-8): 1090-1101.
938 https://doi.org/10.1016/j.agrformet.2010.04.008

939 Pennypacker, S. and Baldocchi, D., 2016. Seeing the fields and forests: Application of surface-
940 layer theory and flux-tower data to calculating vegetation canopy height. Boundary-Layer
941 Meteorology, 158(2): 165-182. https://doi.org/10.1007/s10546-015-0090-0

942 Peñuelas, J., Rutishauser, T. and Filella, I., 2009. Phenology Feedbacks on Climate Change.
943 Science, 324(5929): 887-888. https://doi.org/10.1126/science.1173004

944 Petrie, M.D., Collins, S.L., Swann, A.M., Ford, P.L. and Litvak, M.E., 2015. Grassland to
945 shrubland state transitions enhance carbon sequestration in the northern Chihuahuan
946 Desert. Global Change Biol., 21(3): 1226-1235. https://doi.org/10.1111/gcb.12743

947 Pitman, A.J., 2003. The evolution of, and revolution in, land surface schemes designed for
948 climate models. International Journal of Climatology, 23(5): 479-510.
949 https://doi.org/10.1002/joc.893

950 Qualls, R.J. and Brutsaert, W., 1996. Effect of vegetation density on the parameterization of
951 scalar roughness to estimate spatially distributed sensible heat fluxes. Water Resources
952 Research, 32(3): 645-652. https://doi.org/10.1029/95wr03097

953 Raupach, M.R., 1994. Simplified expressions for vegetation roughness length and zero-plane
954 displacement as functions of canopy height and area index. Boundary-Layer
955 Meteorology, 71(1-2): 211-216. https://doi.org/10.1007/Bf00709229

Raupach, M.R. and Finnigan, J.J., 1988. Single-layer models of evaporation from plant canopies are incorrect but useful, whereas multilayer models are correct but useless: Discuss. Aust. J. Plant Physiol., 15: 705-716. https://doi.org/10.1071/PP9880705

Rice, J.A., 2007. Mathematical statistics and data analysis. Duxbury advanced series. Thomson/Brooks/Cole, Belmont, CA.

Richardson, A.D. et al., 2012. Terrestrial biosphere models need better representation of vegetation phenology: results from the North American Carbon Program Site Synthesis. Global Change Biol., 18(2): 566-584. https://doi.org/10.1111/j.1365-2486.2011.02562.x

Richardson, A.D. and Hollinger, D.Y., 2005. Statistical modeling of ecosystem respiration using eddy covariance data: Maximum likelihood parameter estimation, and Monte Carlo simulation of model and parameter uncertainty, applied to three simple models. Agr. Forest Meteorol., 131(3-4): 191-208. https://doi.org/10.1016/j.agrformet.2005.05.008

Richardson, A.D. et al., 2018. Tracking vegetation phenology across diverse North American biomes using PhenoCam imagery. Sci. Data, 5: 180028. https://doi.org/10.1038/sdata.2018.28

Richardson, A.D. et al., 2013. Climate change, phenology, and phenological control of vegetation feedbacks to the climate system. Agr. Forest Meteorol., 169: 156-173. https://doi.org/10.1016/j.agrformet.2012.09.012

Rigden, A., Li, D. and Salvucci, G., 2018. Dependence of thermal roughness length on friction velocity across land cover types: A synthesis analysis using AmeriFlux data. Agr. Forest Meteorol., 249: 512-519. https://doi.org/10.1016/j.agrformet.2017.06.003

Roman, D.T. et al., 2015. The role of isohydric and anisohydric species in determining ecosystem-scale response to severe drought. Oecologia, 179(3): 641-654. https://doi.org/10.1007/s00442-015-3380-9

Ruehr, N.K., Law, B.E., Quandt, D. and Williams, M., 2014. Effects of heat and drought on carbon and water dynamics in a regenerating semi-arid pine forest: a combined experimental and modeling approach. Biogeosciences, 11(15): 4139-4156. https://doi.org/10.5194/bg-11-4139-2014

Sakai, R.K., 2000. Observational study of turbulent exchange between the surface and canopy layer over several forest types (Ph.D. Thesis). State University of New York at Albany, Albany, NY, 4780 pp.

Schwartz, M.D., 1992. Phenology and springtime surface-layer change. Monthly Weather Review, 120(11): 2570-2578. https://doi.org/10.1175/1520-0493(1992)120<2570:Passlc>2.0.Co;2

Scott, R.L., Biederman, J.A., Hamerlynck, E.P. and Barron-Gafford, G.A., 2015. The carbon balance pivot point of southwestern US semiarid ecosystems: Insights from the 21st

century drought. Journal of Geophysical Research-Biogeosciences, 120(12): 2612-2624. https://doi.org/10.1002/2015jg003181

Scott, R.L., Hamerlynck, E.P., Jenerette, G.D., Moran, M.S. and Barron-Gafford, G.A., 2010. Carbon dioxide exchange in a semidesert grassland through drought-induced vegetation change. Journal of Geophysical Research-Biogeosciences, 115. https://doi.org/10.1029/2010jg001348

Seyednasrollah, B. et al., 2019a. PhenoCam Dataset v2.0: Vegetation phenology from Digital Camera Imagery, 2000-2018. ORNL DAAC, Oak Ridge, Tennessee, USA. https://doi.org/10.3334/ORNLDAAC/1674

Seyednasrollah, B. et al., 2021. Seasonal variation in the canopy color of temperate evergreen conifer forests. New Phytol., 229(5): 2586-2600. https://doi.org/10.1111/nph.17046

Seyednasrollah, B. et al., 2019b. Tracking vegetation phenology across diverse biomes using Version 2.0 of the PhenoCam Dataset. Sci. Data, 6. https://doi.org/10.1038/s41597-019-0270-8

Shaw, R.H. and Pereira, A.R., 1982. Aerodynamic roughness of a plant canopy - a numerical experiment. Agricultural Meteorology, 26(1): 51-65. https://doi.org/10.1016/0002-1571(82)90057-7

Sonnentag, O. et al., 2011. Tracking the structural and functional development of a perennial pepperweed (Lepidium latifolium L.) infestation using a multi-year archive of webcam imagery and eddy covariance measurements. Agr. Forest Meteorol., 151(7): 916-926. https://doi.org/10.1016/j.agrformet.2011.02.011

Sonnentag, O. et al., 2012. Digital repeat photography for phenological research in forest ecosystems. Agr. Forest Meteorol., 152: 159-177. https://doi.org/10.1016/j.agrformet.2011.09.009

Sugita, M. and Kubota, A., 1994. Radiometrically determined skin temperature and scalar roughness to estimate surface heat-flux. Part II: Performance of parameterized scalar roughness for the determination of sensible heat. Boundary-Layer Meteorology, 70(1-2): 1-12. https://doi.org/10.1007/Bf00712520

Suyker, A.E. and Verma, S.B., 2010. Coupling of carbon dioxide and water vapor exchanges of irrigated and rainfed maize-soybean cropping systems and water productivity. Agr. Forest Meteorol., 150(4): 553-563. https://doi.org/10.1016/j.agrformet.2010.01.020

Suyker, A.E. and Verma, S.B., 2012. Gross primary production and ecosystem respiration of irrigated and rainfed maize-soybean cropping systems over 8 years. Agr. Forest Meteorol., 165: 12-24. https://doi.org/10.1016/j.agrformet.2012.05.021

Tao, Z. et al., 2013. Effect of land cover on atmospheric processes and air quality over the continental United States - a NASA Unified WRF (NU-WRF) model study. Atmospheric Chemistry and Physics, 13(13): 6207-6226. https://doi.org/10.5194/acp-13-6207-2013

1029 Thom, A.S., 1972. Momentum, mass and heat-exchange of vegetation. Quarterly Journal of the
1030 Royal Meteorological Society, 98(415): 124-&. https://doi.org/10.1256/smsqj.41509

1031 Thomas, C.K. et al., 2009. Seasonal hydrology explains interannual and seasonal variation in
1032 carbon and water exchange in a semiarid mature ponderosa pine forest in central Oregon.
1033 Journal of Geophysical Research-Biogeosciences, 114.
1034 https://doi.org/10.1029/2009jg001010

1035 Verhoef, A., DeBruin, H.A.R. and VandenHurk, B.J.J.M., 1997. Some practical notes on the
1036 parameter kB(-1) for sparse vegetation. Journal of Applied Meteorology, 36(5): 560-572.
1037 https://doi.org/10.1175/1520-0450(1997)036<0560:Spnotp>2.0.Co;2

1038 Verma, S., 1989. Aerodynamic resistances to transfers of heat, mass and momentum. In: T.
1039 Black, D. Spittlehouse, M. Novak and D. Price (Editors), Estimation of Areal
1040 Evapotranspiration. International Association of Hydrological Sciences, Vancouver,
1041 B.C., pp. 13-20.

1042 Wharton, S., Falk, M., Bible, K., Schroeder, M. and Paw, K.T., 2012. Old-growth CO2 flux
1043 measurements reveal high sensitivity to climate anomalies across seasonal, annual and
1044 decadal time scales. Agr. Forest Meteorol., 161: 1-14.
1045 https://doi.org/10.1016/j.agrformet.2012.03.007

1046 Yang, K. et al., 2008. Turbulent flux transfer over bare-soil surfaces: Characteristics and
1047 parameterization. Journal of Applied Meteorology and Climatology, 47(1): 276-290.
1048 https://doi.org/10.1175/2007jamc1547.1

1049 Yang, R.Q. and Friedl, M.A., 2003. Determination of roughness lengths for heat and momentum
1050 over boreal forests. Boundary-Layer Meteorology, 107(3): 581-603.
1051 https://doi.org/10.1023/A:1022880530523

1052 Zeng, X.B. and Wang, A.H., 2007. Consistent parameterization of roughness length and
1053 displacement height for sparse and dense canopies in land models. Journal of
1054 Hydrometeorology, 8(4): 730-737. https://doi.org/10.1175/Jhm607.1

1055 Zhao, L., Lee, X.H., Suyker, A.E. and Wen, X.F., 2016. Influence of leaf area index on the
1056 radiometric resistance to heat transfer. Boundary-Layer Meteorology, 158(1): 105-123.
1057 https://doi.org/10.1007/s10546-015-0070-4
1058
1059

Supplementary Information

- Appendix S1 – Comparing PhenoCam G_{cc} to Braodband NDVI
- Table S1 – Additional metadata for study sites
- Table S2 – Multiple linear regression results for model predicting kB^{-1}
- Figure S1 – Comparing kB^{-1} values estimated with and without stability effects
- Figure S2 – Figure comparing of PhenoCam G_{cc} to Broadband NDVI
- Figure S3 – Landcover and example PhenoCam imagery for each site
- Figure S4 – Aerodynamic canopy height results for each site
- Figure S5 – Seasonal patterns in R_{ah}, R_{am}, and R_{bh} for sites not in Figure 1.
- Figure S6 – Timing of seasonal peak and minimum R_{ah} for sites not in Figure 2.
- Figure S7 – Aerodynamic resistance results for US-Tw3
- Figure S8 – Added variable plots for regression results

Appendix S1

We compared PhenoCam G_{cc} time series with broadband NDVI calculated using the approach of Jenkins et al. (2007). We first summed the reflected and incident fluxes (both PPFD and SW) measured data over the day, and then calculated the reflected/incident ratio to determine the flux-weighted daily average "PAR albedo" (or VIS reflectance) and "SW albedo". From these we used Jenkins' formula, to estimate NIR reflectance (NIR reflectance = 2×(SW albedo) – (VIS reflectance)). Then we calculated broadband NDVI (at the daily time step) as:

$$\frac{(NIR\ reflectance) - (VIS\ reflectance)}{(NIR\ reflectance) + (VIS\ reflectance)}$$

The results are shown in Fig. S2, We note that in general the agreement between G_{CC} and broadband NDVI is very strong. In many cases, there is also strong seasonality evident in one or more of the broadband reflectances (i.e., total SW albedo, NIR reflectance, or VIS reflectance), but the periods of vegetation activity are not as easily discerned as with either GCC or broadband NDVI.

Site	PhenoCam	AmeriFlux version	AmeriFlux Download Date	Site Acknowledgements
CA-TP4	turkeypointenf39	AMF_CA-TP4_BASE_HH_4-5	2020-02-04	Natural Sciences and Engineering Research Council of Canada (NSERC), Global Water Futures (GWF) Program and Ontario Ministry of the Environment, Conservation and Parks (OECP).
US-Bi1	bouldinalfalfa	AMF_US-Bi1_BASE_HH_2-5	2020-01-10	California Department of Fish and Wildlife
US-Ho1	howland1	AMF_US-Ho1_BASE_HH_6-5	2020-02-11	Research at Howland Forest is supported by the Office of Science (BER), US Department of Energy, and the USDA Forest Service's Northern Research Station
US-Me2	oregonMP	AMF_US-Me2_BASE_HH_9-5	2019-02-14	Support for US-Me2 is provided from the Metolius Core Site Cluster by the DOE Office of Science Ameriflux Network Management Project and by the Office of Science (BER), U.S. Department of Energy, Grant No. DE-FG02-06ER64318.
US-Me6	oregonYP	AMF_US-Me6_BASE_HH_7-5	2020-02-04	Support for US-Me6 is provided from the Metolius Core Site Cluster by the DOE Office of Science Ameriflux Network Management Project and by the Office of Science (BER), US Department of Energy (Award DE SC0005322), and a Leopoldina Research Fellowship to NKR (LPDS 2009-37)
US-MMS	morganmonroe	AMF_US-MMS_BASE_HR_10-5	2019-02-14	Research at the Morgan-Monroe Ameriflux site is supported by the US Departement of Energy, Office of Science, Office of Biological and Environmental Research throuth the Ameriflux Management Project administered by Lawrence Berkeley National Lab
US-MOz	missouriozarks	AMF_US-MOz_BASE_HH_7-1	2019-02-18	The MOFLUX site is supported by Oak Ridge National Laboratory's Terrestrial Ecosystem Science (TES) Scientific Focus Area (SFA), which in turn is supported by the U.S. Department of Energy, Office of Science, Office of Biological and Environmental Research Program, Climate and Environmental Sciences Division.
US-Mpj	usmpj	AMF_US-Mpj_BASE_HH_10-5	2019-04-04	N/A
US-Ne1	mead1	AMF-US-Ne1_BASE_HR_9-5	2020-05-19	N/A
US-Ne2	mead2	AMF-US-Ne2_BASE_HR_9-5	2020-05-19	N/A
US-Ne3	mead3	AMF-US-Ne3_BASE_HR_9-5	2020-05-19	N/A
US-NR1	niwot3	AMF_US-NR1_BASE_HH_12-5	2019-02-14	The US-NR1 AmeriFlux site is currently supported by the U.S. DOE, Office of Science through the AmeriFlux Management Project (AMP) at Lawrence Berkeley National Laboratory under Award Number 7094866.
US-Ro4	rosemountnprs	AMF_US-Ro4_BASE_HH_6-5	2019-08-19	The US-Ro4 AmeriFlux core site is currently supported by the US DOE, Office of Science through the AmeriFlux Management Project (AMP) at Lawrence Berkeley National Laboratory and base funding from USDA-ARS
US-Ses	sevilletashrub	AMF_US-Ses_BASE_HH_10-5	2019-04-04	Support is provided by the Sevilleta Field Station and the University of New Mexico
US-Syv	sylvania	AMF_US-Syv_BASE_HH_12-5	2019-04-04	Support for US-Syv is provided from the ChEAS Core Site Cluster by the DOE Office of Science Ameriflux Network Management Project
US-Ton	tonzi	AMF_US-Ton_BASE_HH_10_5	2019-04-04	This research was supported by the US Department of Energy Terrestrial Carbon Program, grant No. DE-FG03-00ER63013 and DE-SC0005130 and in part by the Office of Science (BER), U.S. Department of Energy, Grant No. DE-FG02-03ER63638
US-Tw3	twitchellalfalfa	AMF_US-Tw3_BASE_HH_5-5	2020-02-04	Biometeorology Lab, University of California, Berkeley, PI: Dennis Baldocchi and California Department of Water Resources, DOE AmeriFlux; Biometeorology Lab, University of California, Berkeley, PI: Dennis Baldocchi
US-UMB	umichbiological	AMF_US-UMB_BASE_HH_12-5	2019-04-04	Primary support for the University of Michigan AmeriFlux Core Site (US-UMB) provided by the Department of Energy Office of Science. Infrastructure support provided by the University of Michigan Biological Station.
US-Var	vaira	AMF_US-Var_BASE_HH_11-5	2019-02-14	This research was supported in part by the Office of Science (BER), U.S. Department of Energy, Grant No. DE-FG02-03ER63638
US-WCr	willowcreek	AMF_US-WCr_BASE_HH_15-5	2019-02-18	Research at the Willow Creek Ameriflux core site is provided by the Dept. Of Energy Office of Science to the ChEAS Cluster
US-Whs	luckyhills	AMF_US-Whs_BASE_HH_12-5	2019-06-12	Research at Walnut Gulch Experimental Watershed is funded by the USDA-ARS. The Lucky Hills and Kendall Ameriflux core sites are also supported by the Dept. Of Energy Office of Science
US-Wkg	kendall	AMF_US-Wkg_BASE_HH_13-5	2019-06-12	
US-Wrc	windriver	AMF_US-Wrc_BASE_HH_8-1	2020-02-04	Data and logistical support were provided by the US Forest Service Pacific Northwest Research Station and the University of Washington

Table S1. Additional metadata for study sites.

Table S2. Summary results from multiple linear regression predicting kB^{-1} at US-Wkg as function of the following variables: net radiation (R_n), latent heat flux (LE), surface temperature (T_s), soil water content (SWC), wind speed (u), and cumulative 10-day precipitation (P_{10}). This regression model was conducted to investigate the influence of different meteorological factors on kB^{-1}. The entire time series of US-Wkg was used, and there were no interactions included in this regression model. Individual observations in the model were non-overlapping 3-day values for each variable. Significance levels: * = 0.05, ** = 0.01, and *** = 0.001.

	Estimate	*SE*	*t*-value	*p-value*
Intercept	-0.7548	0.4015	-1.88	0.061
R_n	0.0017	0.0010	1.80	0.072
LE	-0.0043	0.0018	-2.36	0.018*
T_s	0.1472	0.0115	12.84	<0.001***
SWC	-0.0372	0.0169	-2.20	0.028*
u	-0.0707	0.0383	-1.84	0.066
P_{10}	0.0053	0.0064	0.84	0.403

Number of observations: 706*, Error degrees of freedom:* 699
Root Mean Squared Error: 1.95
R^2 = 0.442
F-statistic vs. constant model: 94.1*, p-value* < 0.001

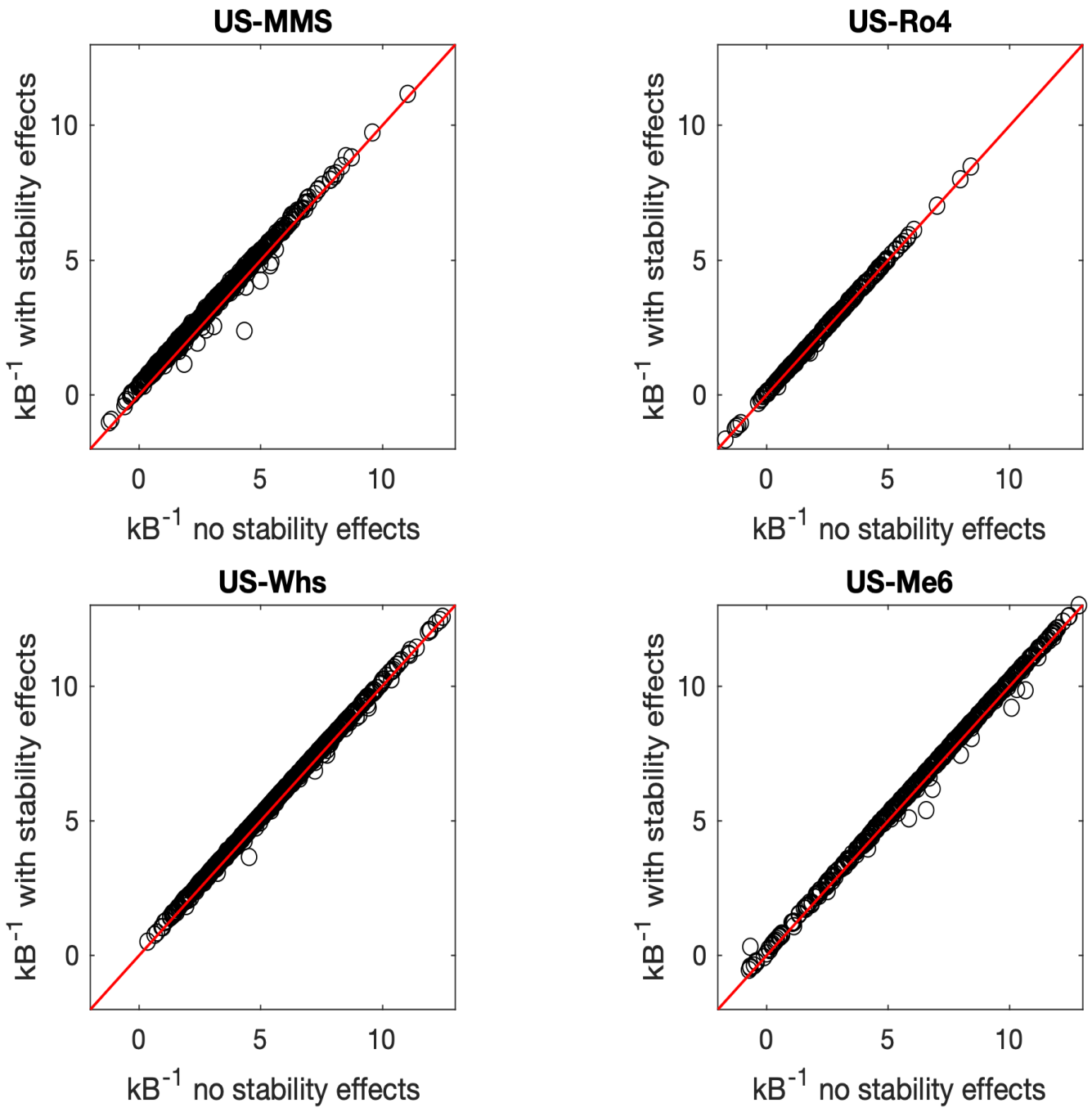

Figure. S1. Comparison between kB-1 estimated when including stability effects vs. no stability effects (Eqns. 4 vs. 5 in main text) for select sites.

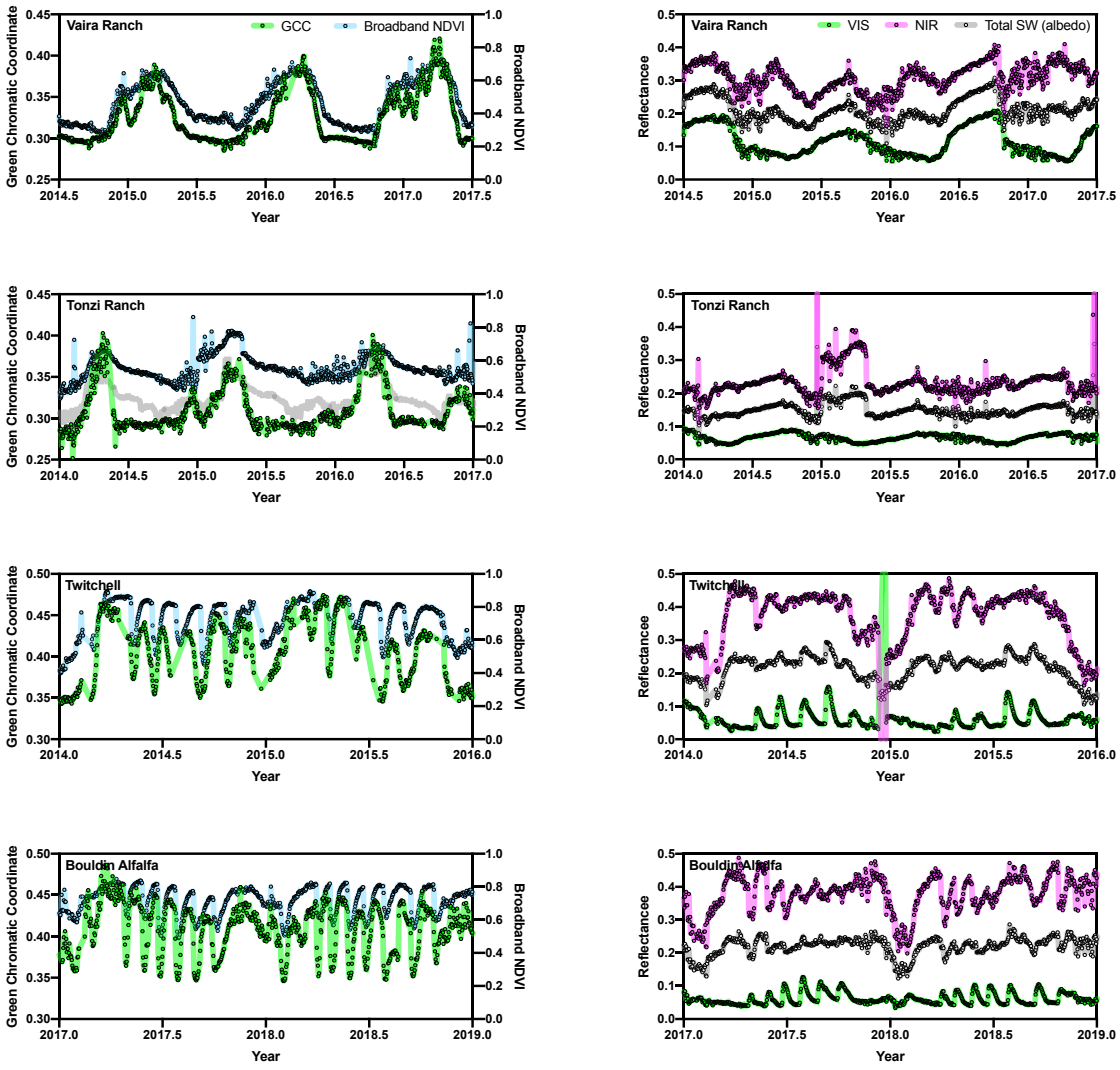

Figure S2. Time series of PhenoCam-derived green chromatic coordinate (GCC) and radiometrically-derived Broadband NDVI (left), and total SW albedo, NIR reflectance, and VIS reflectance (right). For the GCC time series, the primary vegetation type is shown as green symbols. For Tonzi Ranch, a Mediterranean woody savanna, the green symbols indicate the seasonal patterns of GCC for the understory grasses, while the gray line indicates the seasonal patterns of GCC for the overstory deciduous oak trees, *Quercus douglasii*. For each site, three years of data were arbitrarily chosen from the period of overlap between phenocam and radiometric measurements, except for the Twitchell and Bouldin Alfalfa sites for which only 2 y of data are shown due to facilitate visualization of the dynamic harvesting/regrowth patterns.

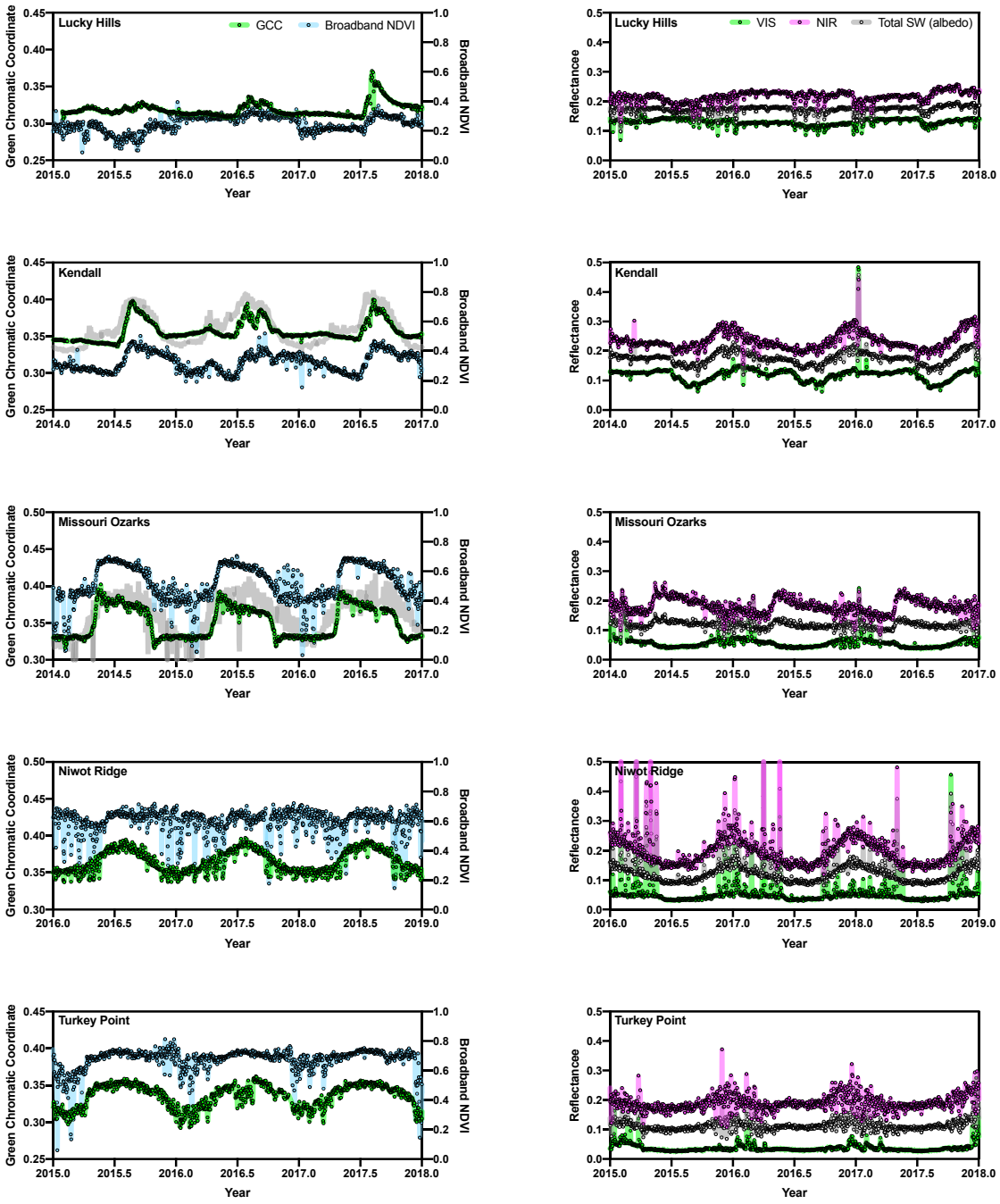

Figure S2 (continued). Time series of PhenoCam-derived green chromatic coordinate (GCC) and radiometrically-derived Broadband NDVI (left), and total SW albedo, NIR reflectance, and VIS reflectance (right). For the GCC time series, the primary vegetation type is shown as green symbols. For Kendall, an arid grassland with some shrub cover, the green symbols indicate the seasonal patterns of GCC for the grass, while the gray line indicates the seasonal patterns of GCC for the shrubs. For Missouri Ozarks, a temperate mixed forest with an evergreen conifer component, the green symbols indicate the seasonal patterns of GCC for the deciduous trees, while the gray line indicates the seasonal patterns of GCC for the evergreen trees. For each site, three years of data were arbitrarily chosen from the period of overlap between phenocam and radiometric measurements.

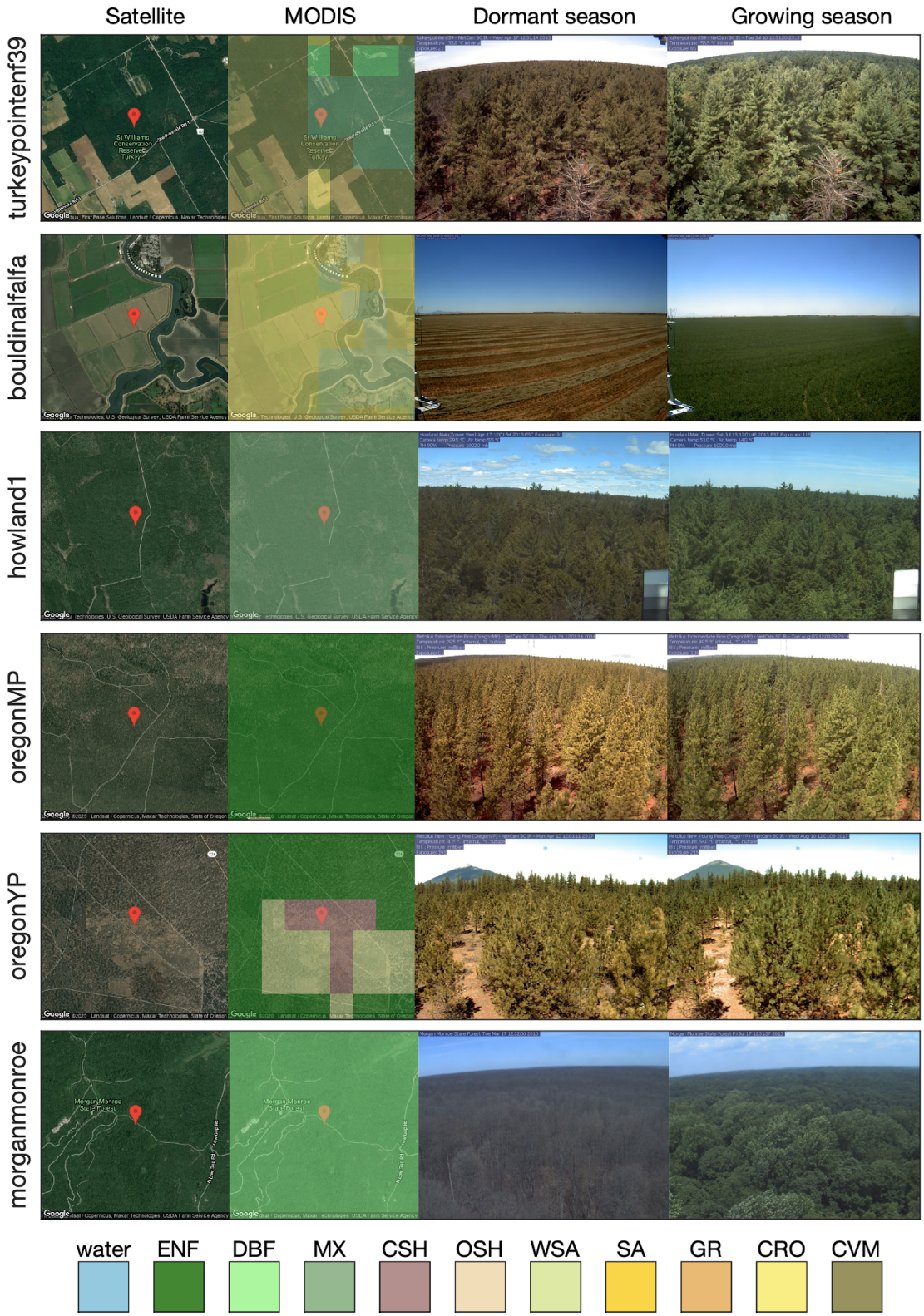

Figure S3. Land-cover and example imagery from PhenoCam for each study site. MODIS data are from the MCD12Q1 product. Codes for the land-cover classes are: ENF = evergreen needleleaf forest, DBF = deciduous broadleaf forest, MX = mixed forest, CSH = close shrublands, OSH = open shrublands, WSA = woody savanna, SA = savanna, GR = grasslands, CRO = agricultural, CVM = crop-natural vegetation mosaic.

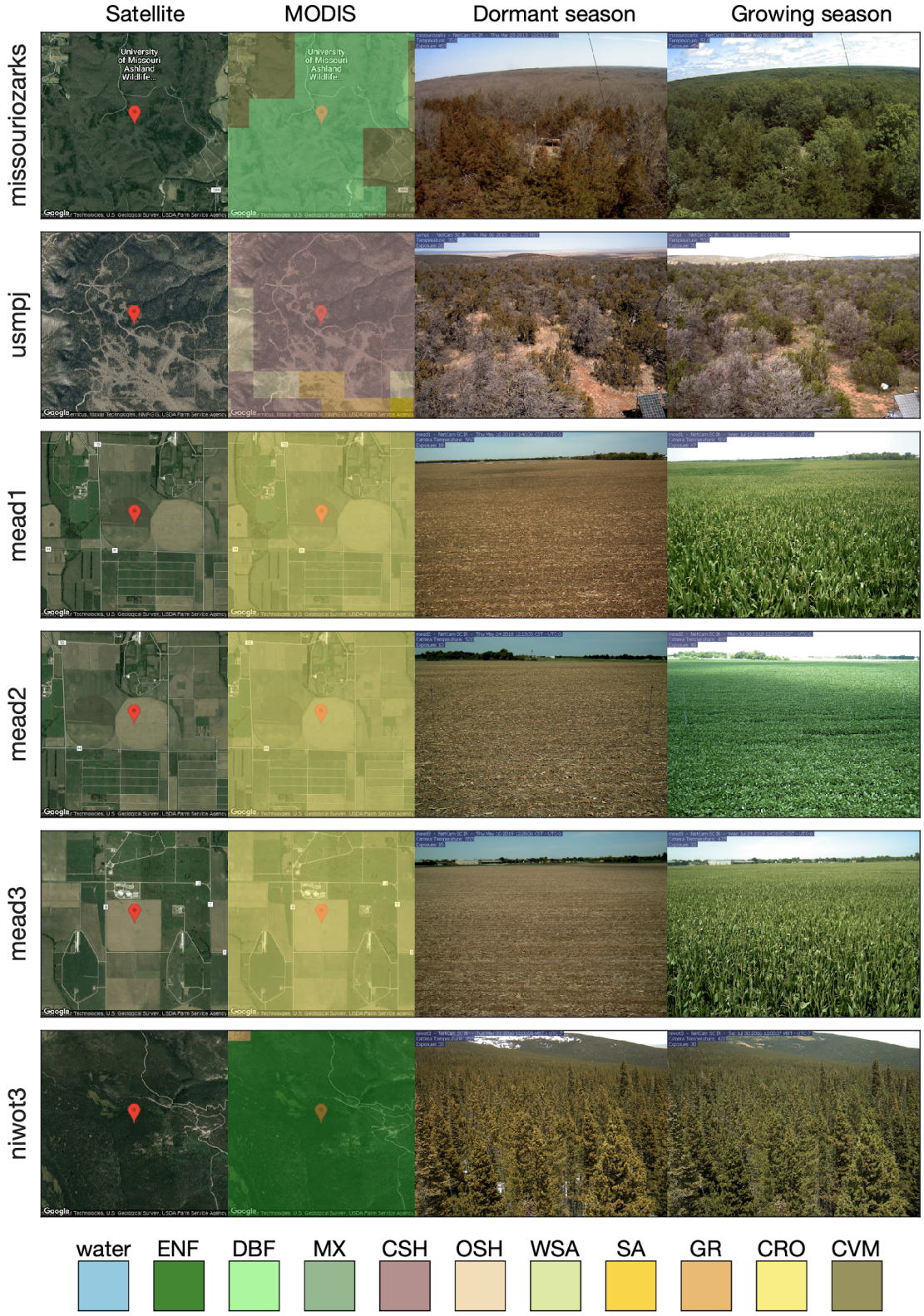

Figure S3 Continued.

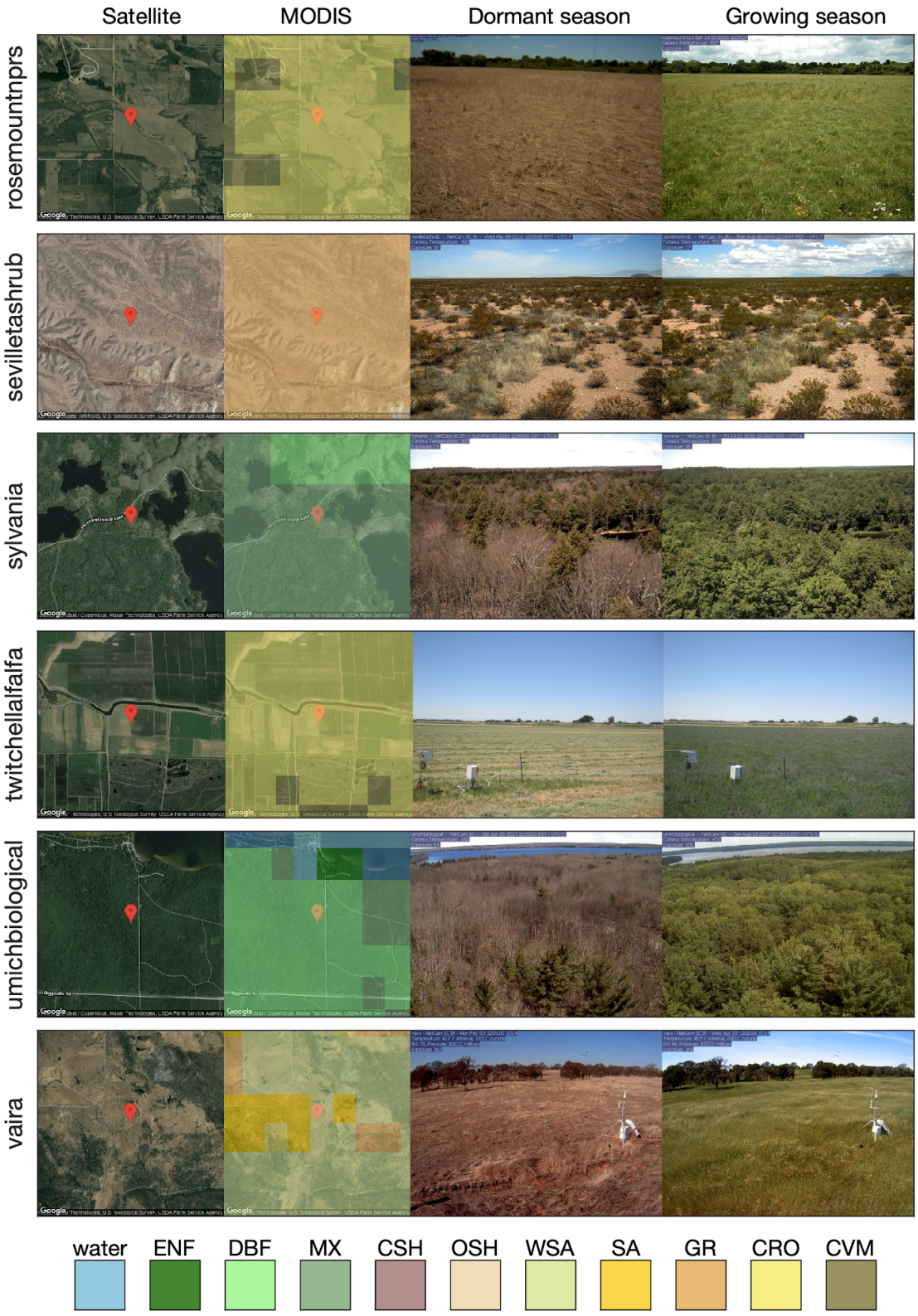

Figure S3 Continued.

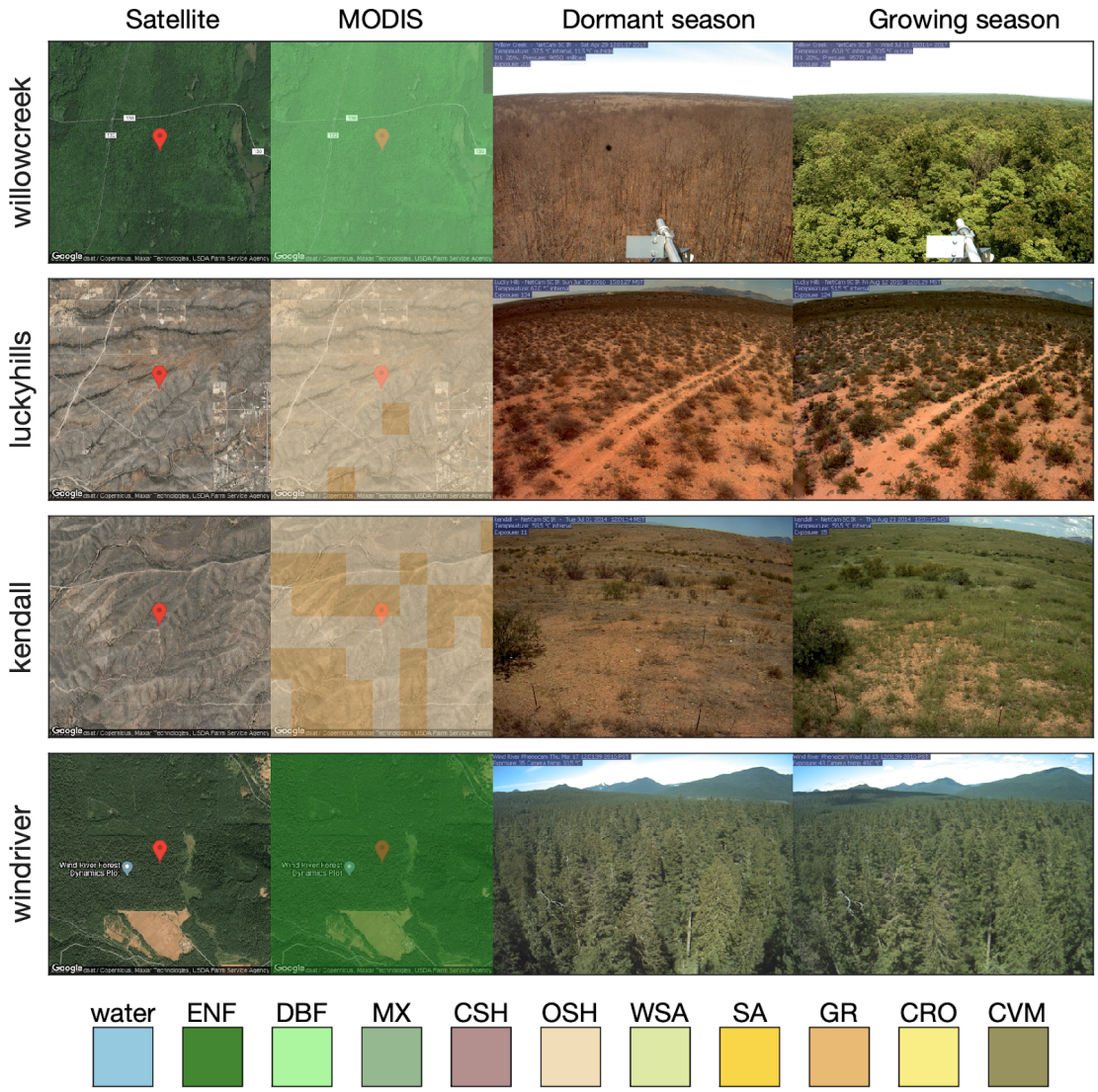

Figure S3 Continued.

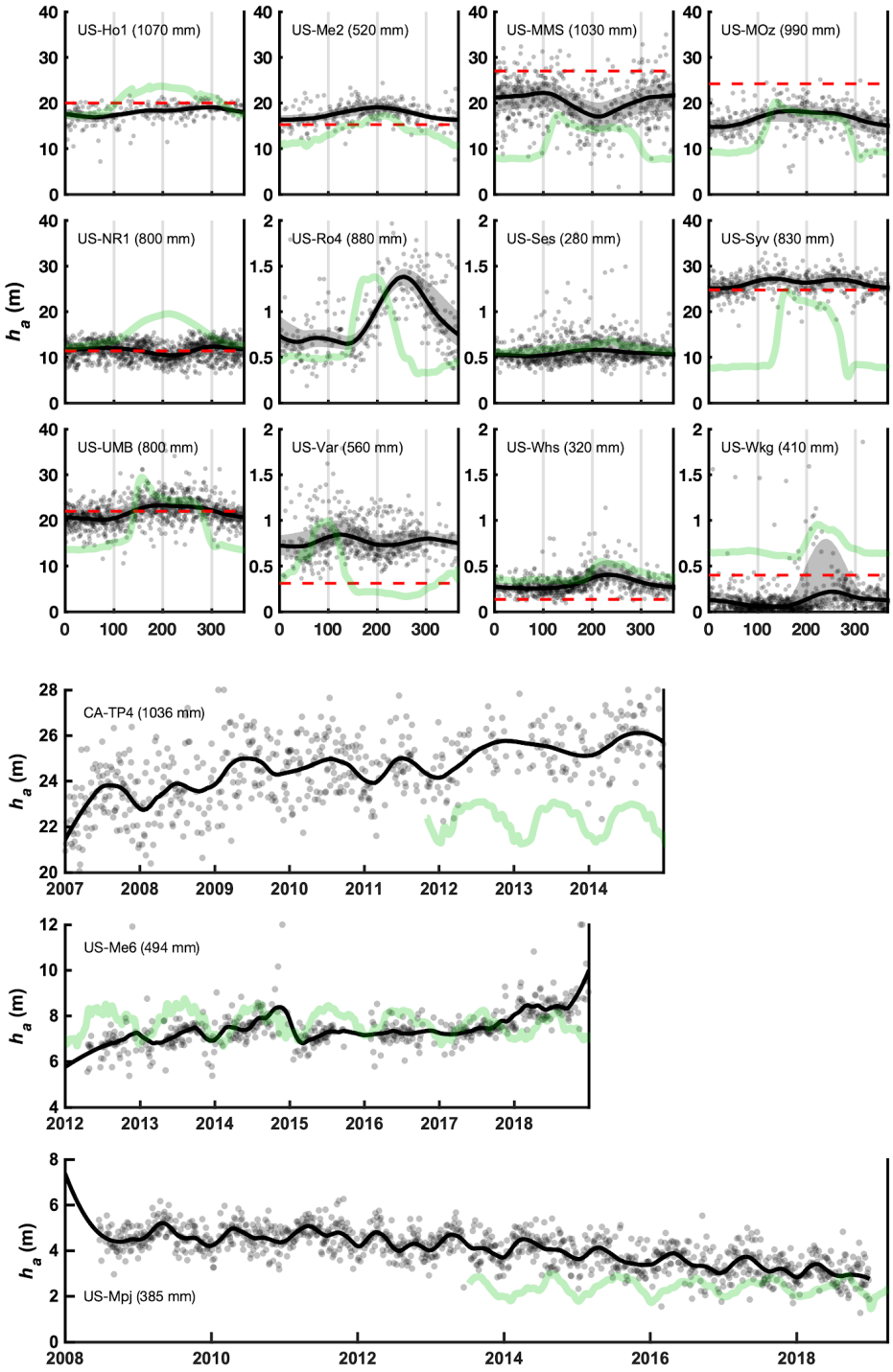

Figure S4. Seasonal changes in aerodynamic canopy height (h_a) for each non-agricultural site. mean annual precipitation (in parentheses next to each site name). For each site, the median and interquartile values (25th and 75th percentiles) are calculated for each DOY across all years, these statistics are then smoothed using a loess smoother. Green lines represent mean PhenoCam GCC across all site years, and the GCC scale is the same across all panels. Horizontal red lines represented PI reported canopy height. The bottom three sites (CA-TP4, US-Me6, and US-Mpj) were plotted as time series due to observed trends in changing h_a.

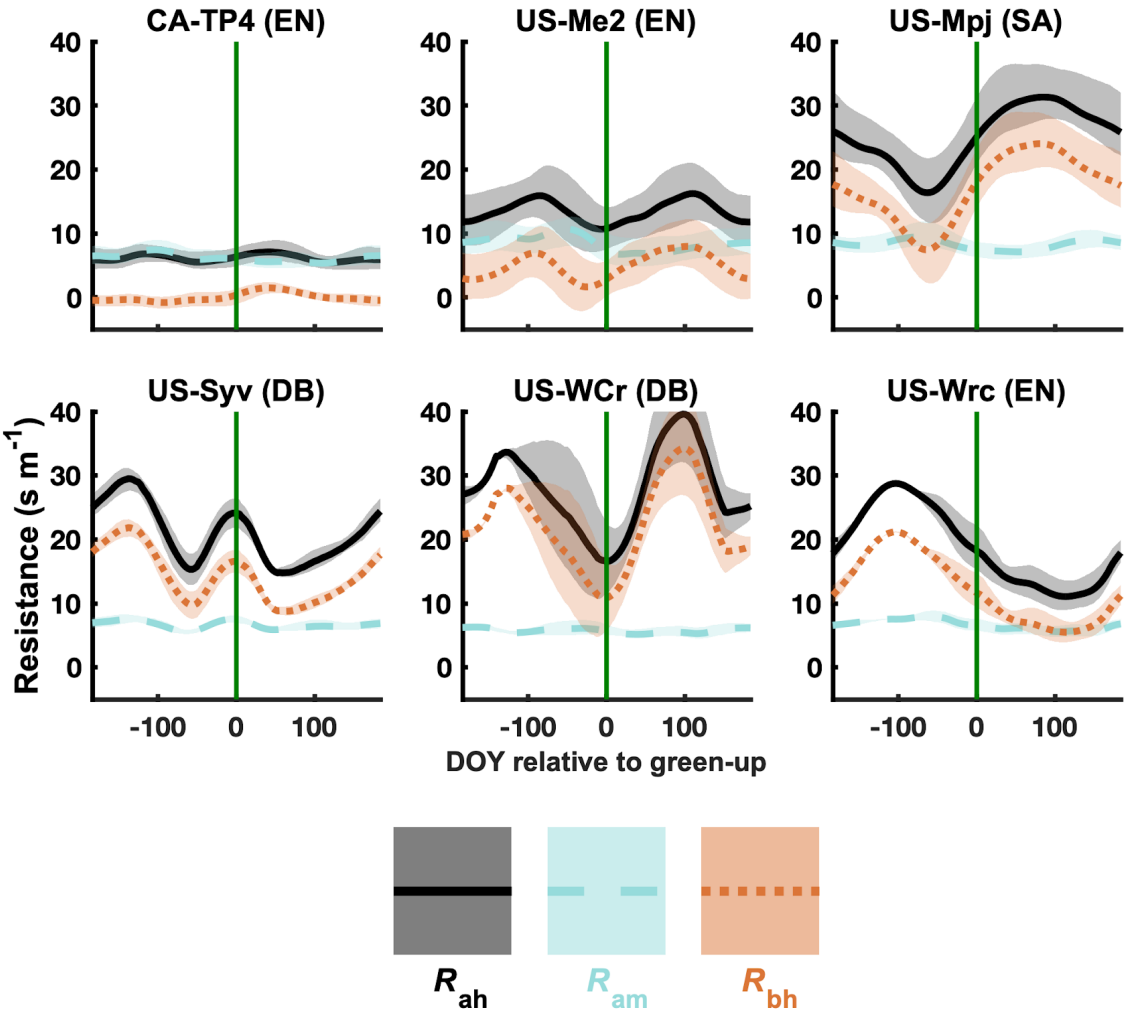

Figure S5. Seasonal changes in R_{ah}, R_{am} and R_{bh} for remaining sites not in Fig. 2. For each site, the median and interquartile values (25th and 75th percentiles) are calculated for each DOY across all years, and these statistics are then smoothed using a loess smoother.

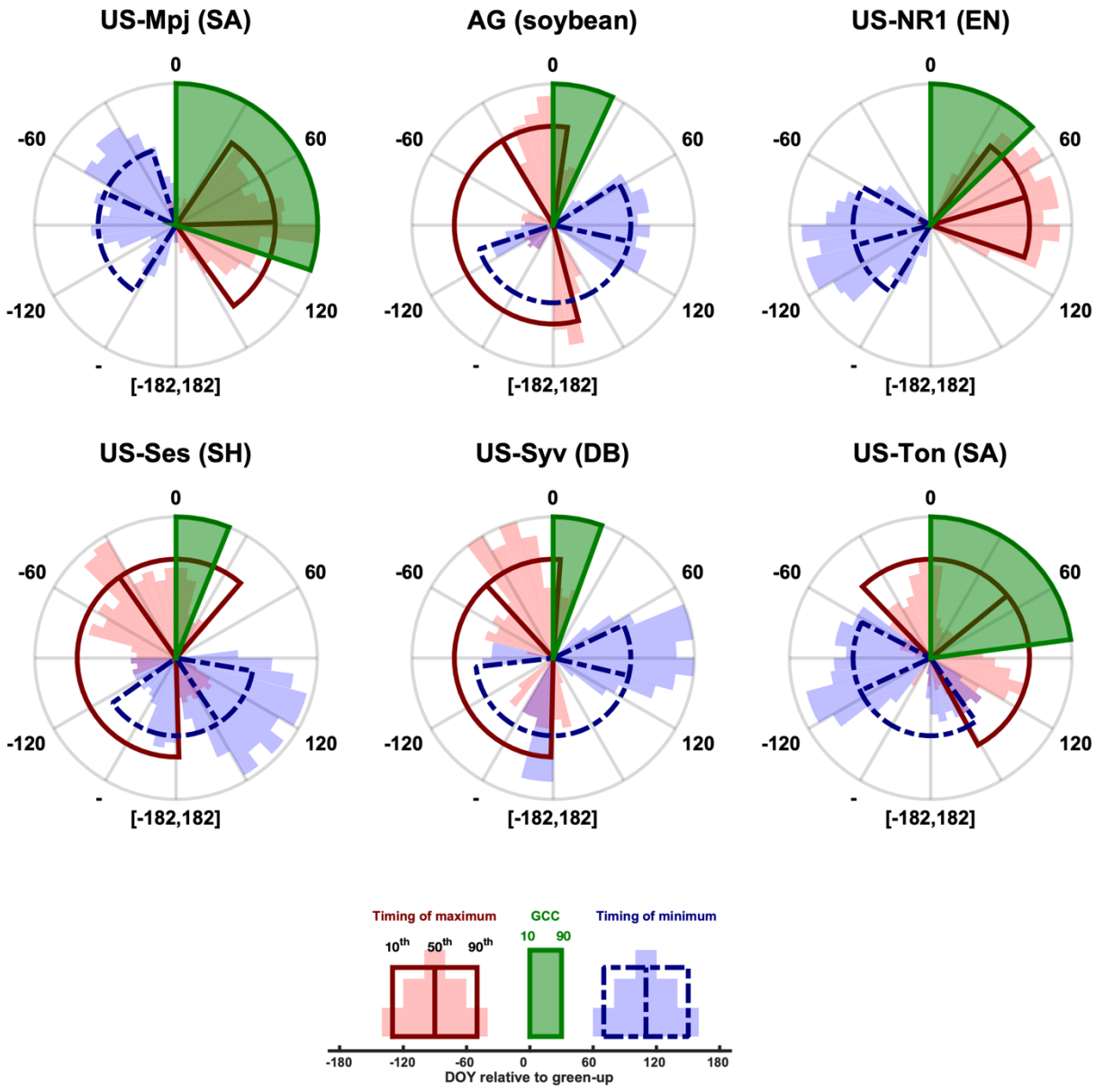

Figure S6. Timing of seasonal maximum and minimum values for aerodynamic resistance to heat transfer (R_{ah}) for additional sites. Red and blue histograms display the empirical distribution of the seasonal maximum or minimum timing, respectively. Day 0 (at the top of each plot) represents start-of-season green-up. These empirical distributions of maximum or minimum timings are summarized by the 10th, 50th, and 90th percentiles of these relative day-of-year values. The green "slices" represent the green-up phenological transition period, bounded by dates when the GCC curve reaches 10% and 90% of the total seasonal amplitude of GCC.

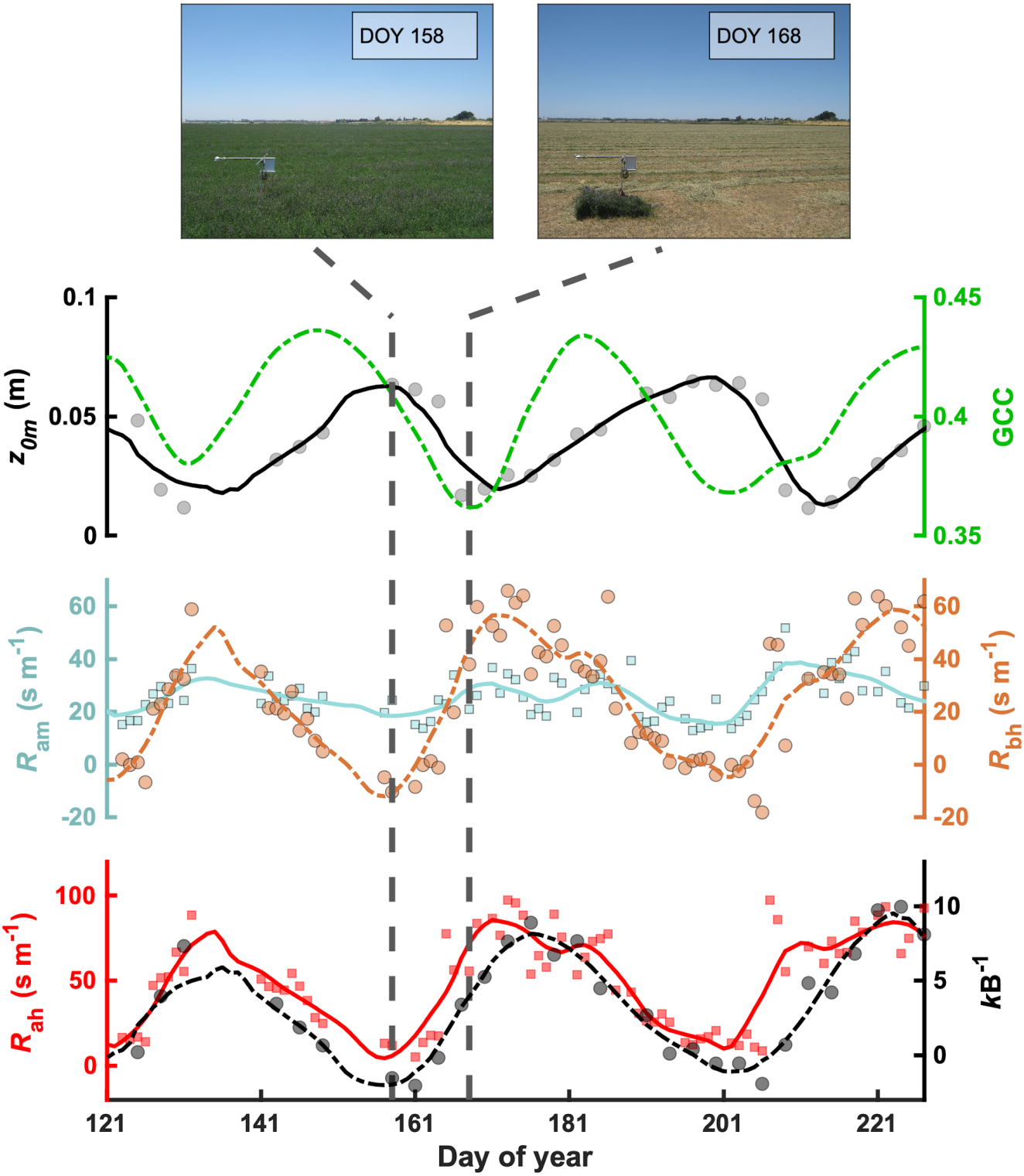

Figure S7. Growing season patterns in roughness length for momentum (z_{0m}), GCC, R_{am}, R_{bh}, R_{ah}, and kB^{-1} for an agricultural site (US-Tw3) for 2014. Images are from the PhenoCam site *twitchellalfalfa* at midday. Due to the short time period, these data are daily (individual points) and smoothed using a loess. Solid and dashed lines represent the smoothed values for the left and right y axes, respectively.

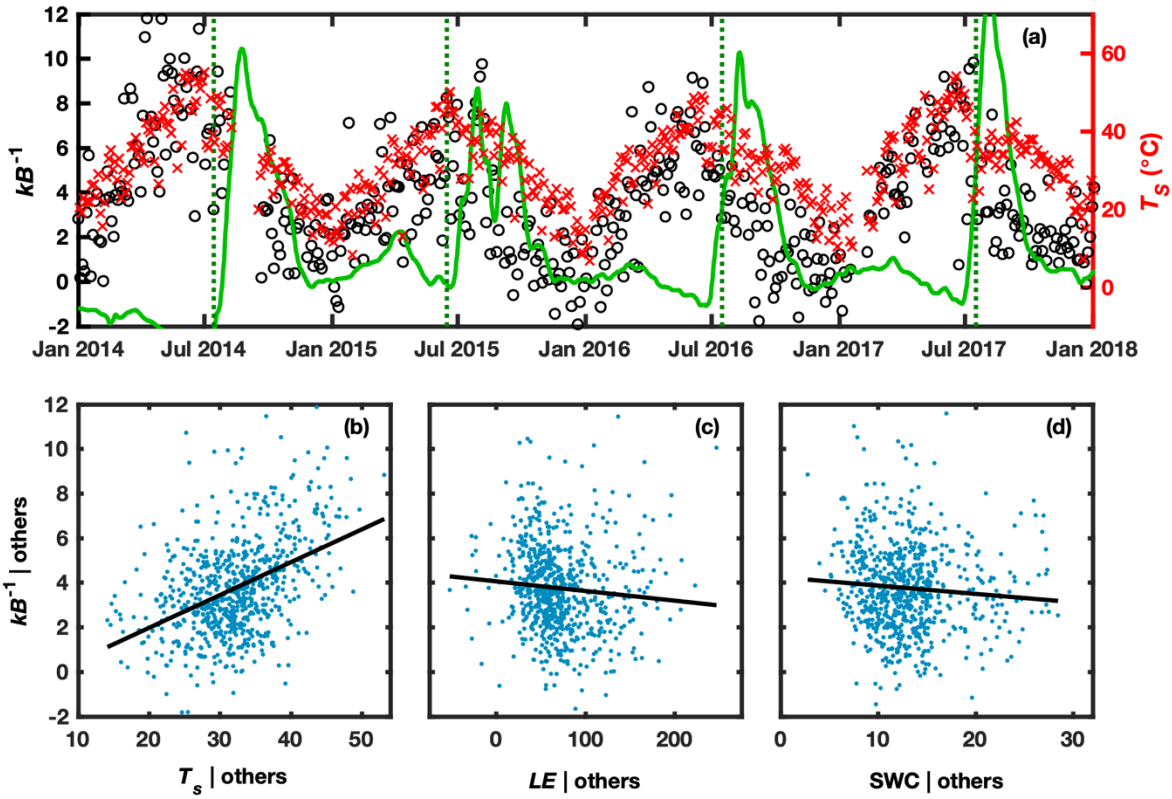

Figure S8. Time series of kB^{-1}, surface temperature (T_s), and PhenoCam greenness at US-Wkg (a). Added-variable plots depicting partial relationships between kB^{-1} and the three explanatory variable to emerge as significant at the $\alpha = 0.05$ significance level in our regression analysis (Table S2): T_s (b), *LE* (c), and soil water content (d). Vertical lines indicate PhenoCam green-up dates.